



저작자표시-비영리-변경금지 2.0 대한민국

이용자는 아래의 조건을 따르는 경우에 한하여 자유롭게

- 이 저작물을 복제, 배포, 전송, 전시, 공연 및 방송할 수 있습니다.

다음과 같은 조건을 따라야 합니다:



저작자표시. 귀하는 원저작자를 표시하여야 합니다.



비영리. 귀하는 이 저작물을 영리 목적으로 이용할 수 없습니다.



변경금지. 귀하는 이 저작물을 개작, 변형 또는 가공할 수 없습니다.

- 귀하는, 이 저작물의 재이용이나 배포의 경우, 이 저작물에 적용된 이용허락조건을 명확하게 나타내어야 합니다.
- 저작권자로부터 별도의 허가를 받으면 이러한 조건들은 적용되지 않습니다.

저작권법에 따른 이용자의 권리는 위의 내용에 의하여 영향을 받지 않습니다.

이것은 [이용허락규약\(Legal Code\)](#)을 이해하기 쉽게 요약한 것입니다.

[Disclaimer](#)

공학박사 학위논문

A platform study for transport
modeling of external materials
using microfluidics chips

신체 외부 물질의 전달 모델링을 위한
미세유체칩 플랫폼 연구

2023년 2월

서울대학교 대학원

공과대학 재료공학부

황 혜 원

A platform study for transport modeling of external materials using microfluidics chips

지도 교수 선정윤

이 논문을 공학박사 학위논문으로 제출함
2023년 1월

서울대학교 대학원
공과대학 재료공학부
황 혜 원

황혜원의 공학박사 학위논문을 인준함
2023년 1월

위 원 장 도 준 상 (인)

부위원장 선 정 윤 (인)

위 원 강 승 균 (인)

위 원 옥 명 렬 (인)

위 원 이 효 진 (인)

Abstract

In the development and utilization of materials in the field of medical engineering, research using various bio-friendly materials such as device-based research and nanocarrier utilization is being conducted. Therefore, it is necessary to understand the behavior of an external substance when it is injected into the body. Molecular substances typically occur at very local sites, and in order to verify their effectiveness, nanocarriers injected into blood vessels reach lesions from blood vessels, so they can accurately predict how much of the drug is actually distributed to cancer tissues. Therefore, in this study, we studied the in vitro platform, an advanced form that can use microfluidic chips and conduct material transfer research considering the characteristics of the materials. The chip was modified in a form applicable to the Solution of Fick's second law, and the experiment was designed to conduct transport research on the microfluidic chip.

First, for a specific purpose, the behavior of active oxygen (ROS) generated on the surface of the implanted material in the body was studied. Based on the chemical measurement technology of ROS, the concentration of hydrogen peroxide (H_2O_2) passing through fibrin, one of the extracellular substrates, was measured inside the microfluidic chip, and the diffusion coefficient of H_2O_2 was calculated by reflecting its self-degradation rate. It also showed the concentration distribution of H_2O_2 in tissue by showing the degree of cell-induced consumption in fibrin matrix including cells as well as

simple fibrin and presented a platform to predict the spatiotemporal distribution of molecules generated on the surface of implant materials.

In the second study, diffusivity of mesoporous silica nanoparticle (MSN), which is more highly utilized in biomedical fields, in collagen was studied using microfluidic chips. MSN diffusion inside the chip was captured by simulating the blood flow rate with an easy technique for imaging six-sized MSNs attached with fluorescent substances at a specific time. The diffusion coefficient was calculated based on the fluorescent image and the values were quantitatively expressed. Through this, a platform capable of predicting the spatiotemporal distribution of nanocarriers from outside the blood vessel with accurate values was presented.

The third study introduced human umbilical vein endothelial cell (HUVEC) and modeled using a 5-channel chip for vascular formation and a 3-channel chip for diffusion calculation from the actual blood vessels to the diffusion process through the vessel wall. It was confirmed whether MSN of six sizes passed through the vessel wall, and the passage rate of three representative sizes was calculated through image analysis. In addition, MSN diffusion coefficients of all sizes in the mixed matrix of fibrin and collagen were calculated by the same imaging analysis method as in the previous study. Here, through comparison with animal experiments, it is considered a reliable platform as the results of simulation on this platform show that the tendency is somewhat consistent.

In conclusion, this paper designed microfluidics chips to calculate the

diffusion coefficient by fitting it to the solution of Fick's second law and set the experimental conditions to enable a transport study of injection external materials. The platforms that can understand the transport process step by step was developed and are highly utilized in that various materials can be used instead of the materials used in this study. It is expected to be used as a platform for initial screening tests such as interaction with blood vessels and extracellular substrates of materials developed at the time of pre-development, and various transport studies can be conducted through spheroids or organoids.

Keywords: transport, modeling, microfluidics chip, biomolecule, nanocarrier

Student Number: 2016-26930

Table of Contents

Abstract.....	i
List of Figures.....	v
Chapter 2	vii
Chapter 3	viii
Chapter 4	xii
Chapter 1. Introduction	1
1.1 Study Background.....	1
1.2 Purpose of Research.....	3
Chapter 2. Generation and Diffusion of Biomolecules	4
2.1 Introduction.....	4
2.2 Experimental Procedures	7
2.2.1 Kinetics of second order reaction of H_2O_2 degradation	7
2.2.2 Solution of Fick's second law at constant boundary condition.....	7
2.2.3. Chip designs and fabrication.....	8
2.2.4. HUVECs culture.....	12
2.2.5. Fibrin gel clotting and HUVECs embedding ...	12
2.2.6. H_2O_2 infusion.....	15
2.2.7. H_2O_2 concentration measurement	16
2.2.8. H_2O_2 degradation measurement	16
2.2.9. Immunostaining.....	16
2.3 Results and Discussion	18
2.3.1 Fibrin matrix characterization	18
2.3.2 Self-degradation of H_2O_2	18
2.3.3. H_2O_2 diffusion coefficient (D)	21
2.3.4. H_2O_2 Consumption by cells.....	23
2.3.5 Cell response against H_2O_2 gradient.....	26

2.4 Conclusion	28
Chapter 3. Diffusion of Nanocarriers	29
3.1 Introduction.....	29
3.2 Experimental Procedures	34
3.2.1. Materials.....	34
3.2.2 Preparation of MSNs	34
3.2.3 Measurement of Raman spectra	35
3.2.4 Chip fabrication.....	35
3.2.5 Channel coatings.....	36
3.2.6 Collagen preparation and gel insertion	36
3.2.7 Connection of LOC to the syringe pump.....	37
3.2.8 Collagen Dying and mesh imaging.....	39
3.2.9 Image analysis	39
3.2.10 Diffusion model.....	40
3.2.11 Statistics	41
3.3 Results and Discussion	42
3.3.1 Characterization and preparation of MSNs.....	42
3.3.2 Confirmation of diffusion capability of MSNs in collagen matrix	46
3.3.3 Experimental realization of boundary conditions and acquisition of concentration gradient data	49
3.3.4 Calculation of diffusion coefficient (D)	54
3.3.5 Diffusion profiles of MSNs and their applications	58
3.4 Conclusion	63
Chapter 4. Transport of Nanocarriers.....	65
4.1 Introduction.....	65
4.2 Experimental Procedures	67
4.2.1. Materials.....	67
4.2.2. MSNs fabrication	67
4.2.3. Chip fabrication and channel coatings.....	68
4.2.4. Cell preparation	69
4.2.5. Gel preparation and cell embedding.....	70

4.2.6. Perfusion preparation	72
4.2.7. Gel dyeing and mesh imaging	74
4.2.8. Cell and MSNs imaging	74
4.2.9. Connection of the chip to the syringe pump...	74
4.2.10. Image analysis	75
4.2.11. Diffusion model	75
4.2.12. Drug efficiency	76
4.3 Results and Discussion	78
4.3.1. Fibrin and collagen mixture matrix	78
4.3.2. Vessel formation in three types of gels	80
4.3.3. MSNs characterization	83
4.3.4. MSNs penetration through vessel walls	85
4.3.5. Diffusion coefficient calculation	89
4.3.6. Animal testing results	92
4.3.7. Comparison of drug efficiency and concentration profile	94
4.4 Conclusion	96
Chapter 5. Conclusion	97
References	99
Abstract in Korean (국문 초록)	105

List of Figures

Chapter 2

Figure 2.1. Images of self-degradation and cell consumption of H_2O_2 in a tissue that consists of extracellular matrix and cells.

Figure 2.2. (a) The manufacture of microfluidics chips. (b) The produced microfluidics chip used in this investigation, with varying reservoir sizes (8 mm and 1 mm diameter, respectively)

Figure 2.3. An overview of the chip's structure. The diffusion direction changes from left to right channel. The reservoir size was changed to provide for more exact boundary conditions in the solution of Fick's second law.

Figure 2.4. Images after fibrin injection into the chip's center channel and fibrin + cell mixture injection into the chip's center channel.

Figure 2.5. Dyed pictures of two fibrin concentrations, 2.5 and 5.0 mg/ml, used to compute the diffusion coefficient and self-decomposition rate of H_2O_2 . ImageJ was used to calculate the percentage area of fibrin fibers. ($^{***}p < 0.001$)

Figure 2.6. The degradation of H_2O_2 in fibrin gel is seen schematically on the left. The rate of H_2O_2 decomposition was monitored at 30-minute intervals and is graphed on the right. The graph illustrates that a higher fibrin concentration of 5.0 mg/mL results in a faster degradation rate.

Figure 2.7. H_2O_2 concentration after diffusion and concentration patterns in two types of gels were measured. The concentration of fibrin from the output reservoir was monitored every 45 minutes for 3 hours at 2.5 mg/mL and 5.0

mg/mL. $C(x, t)$ values were shown below the concentration graphs using the calculated D .

Figure 2.8. (Left) Fibrin concentration detected in cell outflow reservoir. (Right) The extinction rates of HUVEC and fibrin itself can be calculated from the extinction rates of tissue. The cell-containing matrices (tissue and HUVEC) were treated as meaningless when the value at $t = 0$ was stated.

Figure 2.9. H_2O_2 distribution in cell-containing tissue over 45, 90, 135, and 180 minutes. When compared to the initial concentration, the concentration at $x = 2.0$ mm is less than 20%.

Figure 2.10. The HUVEC reaction to the H_2O_2 gradient in the matrix. When the region was partitioned into three pieces, the cell response differed when an H_2O_2 gradient was established. HUVECs in section 1 tend to show apoptosis three hours after being injected with 200 M of H_2O_2 , whereas HUVECs in section 3 prefer to aggregate to form vessels.

Chapter 3

Figure 3.1. The tumor microenvironment and microfluidics chips are depicted schematically. The blood vessel and ECM in the left image correspond to the same portion of the chip as seen in the right image.

Figure 3.2. (a) An example of a perfusion chip with inlets and outputs. On, an optical picture of the chip's inside is taken (b). After injecting collagen gel and PBS into peripheral channels, the gel-liquid interface (yellow dotted box)

developed. TEOS and PDA were used to coat the left and center channels, respectively. (c) The connection between the syringe pump and the gel-injected microfluidics chips. During the perfusion, the chips were put in a humidified incubator for 3 hours. 3D representation of the chip is presented on (d).

Figure 3.3. The TEM images of MSNs. The diameters are 10 nm (a), 45 nm (b), 100 nm (c), 200 nm (d), 500 nm (e), and 1 μ m (f), respectively.

Figure 3.4. (a) Based on the images, the average particle size was also obtained. (b) In addition, the physical properties of each particle are displayed in. (c) The particles' zeta potential was also measured. (d) MSN fluorescence intensity was also measured.

Figure 3.5. 0.2% collagen mesh and homogeneity. (a) Injected collagen (0.2%) into the chip's central channel. Alexa Fluor[®] 555 NHS Ester (ex: 555 nm/em: 572 nm) was used to stain the collagen fiber. (b) A greater magnification picture of collagen fibers. The collagen mesh size appears to be 10 μ m. (c) The 3D fiber structure of homogenous collagen gel was detected using z-stacking.

Figure 3.6. The chemical structure of polydopamine (PDA), as well as the non-coated and coated polydopamine channels. Due to PDA shrinking issues, collagen was detached from the channel if the PDA coating was not done in the channel. The collagen structure was physically preserved when the PDA coating was applied.

Figure 3.7. MSNs diffuse in the chip's collagen matrix. Schematic of induced

diffusion in the chip. MSN diffusion coefficients were calculated using the square boxed region. Fluorescence-tagged particles moved at a steady rate in the left channel, whereas particle-free PBS moved at the same rate in the right.

Figure 3.8. To prevent MSN aggregation, TEOS coating was applied within the left channel. Without the coating method. MSNs clustered together, making it difficult to obtain distinct diffusion pictures. However, because there was no aggregation with TEOS coating, clear data were obtained.

Figure 3.9. In the 0.2% collagen gel, a concentration gradient appeared. The green fluorescence intensities of MSNs of various sizes were normalized and fitted with Fick's second law solutions. MSNs of sizes of 10, 100, and 500 nm were displayed.

Figure 3.10. Diffusion coefficients (D) of the MSNs are plotted in bar graphs. ($*p < 0.05$ and $***p < 0.001$)

Figure 3.11. When $t = 3$ hours, 50% or more of the original concentration is dispersed in diverse ways at 100 μm , the distance from the general blood artery to the cancer tissue.

Figure 3.12. The theoretical concentration profiles that can be found within the chip. In order to obtain the most accurate answer from equation (1), it is important that the MSNs do not become completely saturated inside the collagen gel ("Unsaturated," blue line). This allows the collagen gel to be thought of as a semi-infinite medium. When MSNs enter the right channel, which is filled with PBS and has a much faster diffusion rate, the concentration profile, which is denoted by the red line and labeled

"Saturated," does not match the profile that would be ideal, which would be denoted by the red dotted line if the medium were semi-infinite.

Chapter 4

Figure 4.1. Schematic images of tumor microenvironment (TME) and microfluidics chips which could represent microvessel area and mimic diffusional transport.

Figure 4.2. The 5-channel chip for HUVEC culture and 3-channel chip for diffusion study. Both chips were used in this study to model the MSNs penetration and diffusivity.

Figure 4.3. The perfusion method to 5 channel chip. The microvessels were formed in the center channel of the chip (blue channel). When MSNs are applied to the left channel and PBS perfusion is applied to the right channel to the chip on which microvessels have been created for 72 hours, nanoparticles flow into the created vessels.

Figure 4.4. The mixture matrix of collagen (0.1%) and fibrin (0.1%). (a) The dyed mixture was captured with confocal microscopy. (b) The homogeneity of the gel component is proven from the z-stacked images. (c) Higher magnification SEM image was captured to show the collagen and fibrin fiber formed together.

Figure 4.5. Well-formed microvessel in center channel of 5-channel chip. As a result of generating microvessels for 72 hours in the fibrin and collagen

mixture matrix, it was confirmed that vessel formation was good and HUVEC connection was well established.

Figure 4.6. Comparison of microvessel formation in three types of ECM gels.

To form the microvessels with HUVECs, fibrin matrix was adopted to make the well-formed microvessels in vitro. However, we targeted tumor microenvironment, collagen was also mixed with fibrin. The mixture matrix shows the similar tendency of vessel growing, comparing with fibrin only matrix.

Figure 4.7. TEM mages of all sizes of MSNs (10 nm, 45 nm, 100 nm, 200 nm, 500 nm, 1 μ m) were obtained. Also, other features of MSNs such as mean pore size, BET surface area, pore volume and zeta potential were characterized.

Figure 4.8. The endothelial barrier penetration of each size of MSNs. (b) 10 nm and (c) 100 nm MSNs tend to show leakage from the microvessels, but (d) 1 μ m MSNs flow through the microvessel rather than pass through the barrier. (e) The penetration rate was calculated based on (a), (b) and (c). Each group are statistically significant (* $p < 0.05$, ** $p < 0.01$ and *** $p < 0.001$).

Figure 4.9. Confocal microscopy images of each size of MSNs were captured to show X-Y plane and cross-section (X-Z or Y-Z planes) so that the leakage from the lumen can be demonstrated. From 10 nm to 200 nm, the number of MSNs located outside of the microvessels. However, for 500 nm and 1 μ m sizes, more MSNs remained inside the vessel, which indicates that the larger size of the particles are hardly able to pass through the vessel barriers. The

yellow arrows indicate the inside the vessel and the cyan arrow indicates the outside of the vessel

Figure 4.10. (a) MSNs perfusion at a flow rate of 450 $\mu\text{l/h}$. (b) The particles of the small size (10, 45 and 100 nm) were perfused for 3 hours, and the particles of the relatively large size (200 nm, 500 nm and 1 μm) were perfused for 6 hours and then imaged. (c) Based on this, gradient is graphed and the result of fitting to the solution of Fick's second law.

Figure 4.11. D of MSNs in ECM including fibrin has a value with an order of 10^{-12} because the mesh size was small. Small sized particles have a relatively high D value. Based on this, the profile at $t = 3$ was plotted by normalizing the initial concentration.

Figure 4.12. Animal testing result with using various sizes of MSNs and not using MSNs. Control group indicates the no drug injection. PTX (paclitaxel) indicates the drug only group. All sizes of the MSNs have the same volume of PTX inside the pore of them (***) $p < 0.001$). MSNs are more effective than simple drugs, and the smaller the size MSNs, the better effect in tumor.

Figure 4.13. Comparing with drug efficiency from animal testing, the modeled system has similar tendency in that the size difference of the particles have different profile as the distance gets farther from the vessel surface.

Chapter 1. Introduction

1.1. Study Background

In the development and utilization of materials in the field of biomedical engineering, research using various biocompatible materials, such as device-based research and nanocarrier utilization, is being conducted[1-3]. Beyond research on simply replacing parts of body functions using biocompatible materials, research on regeneration, treatment, and even diagnosis is now a trend. Typically, devices or materials are inserted into the body in the form of implants to generate biomolecules or release substances to be used for regeneration and treatment[4-6]. A recent research trend is to inject biocompatible materials such as nanocarriers and use them for stable drug delivery. In the biomedical engineering aspect of materials, rather than mere cell-level delivery research, it is necessary to study the body's response to materials generated from devices and directly injected into the body.

Molecular-level substances generated from implant materials are a phenomenon that occurs in a very local area[7-9]. In order to verify the effect, it is necessary to understand the spatial and temporal distribution of the generated molecules. In the case of nanocarriers injected into blood vessels, only a portion reaches the lesion from the blood vessel, so it is necessary to understand how the amount reaching the lesion is distributed in space and time to the cancer tissue in order to accurately predict the actual drug delivery amount.

Biomolecules can be created through bio-implantable materials, and are characterized by being created and destroyed in a relatively short time[10-13].

On the other hand, nanocarriers are substances that are injected directly into the body. They can be intentionally given various functions, reach the body, preserve their function and form, and are characterized by relatively slow disappearance.

Therefore, research on delivery through lab-on-a-chip and microfluidic chip has been progressing. It is easy to manufacture according to the design and can be experimented with in a small amount so that parallel experiments are possible, which is very efficient in terms of time and cost. Therefore, there is also the possibility of evolving the system to allow for some degree of automation. In addition, it is a useful platform for modeling as it can control other variables by implementing a simpler form than actual tissue. It is widely used as a screening platform because there is no ethical problem. The area I focus on is the observation of transport at the distal end after injection, which is very local and in the case of nanocarriers.

Since diffusion accounts for the largest part among them, the transport of biomolecules and nanocarriers with microfluidic chips has been studied with a focus on diffusion. Taking advantage of these chips, I designed my own chips under the experimental conditions I needed to study the transport of biomolecules and nanocarriers mentioned above.

1.2. Purpose of Research

Previously, various related studies have been conducted due to the importance of understanding the transport process. However, previous studies had some limitations. In some cases, research was conducted without understanding the characteristics of material degradation, etc[4, 7, 13]. In addition, transport research has been conducted by utilizing the advantages of the chip, but delivery from blood vessels has not been considered. Also, even when blood vessel research was conducted, delivery research was conducted under conditions that were not suitable for the transport environment, such as coating channels with HUVEC rather than forming actual blood vessels[14-16]. Even if the actual blood vessels were formed and the research was conducted, a lot of phenomenon observation studies were conducted, but there was a limit to not actually modeling them. Based on various excellent studies that have already been conducted, I conducted transport research in a way to make use of the strengths and supplement the limitations by using these studies as references.

Chapter 2. Generation and Diffusion of Biomolecules

2.1. Introduction

Biomolecules are molecules found in our bodies that range in size from small molecules used in cell signaling to large molecules like proteins and polysaccharides[17, 18]. Their common feature is that they exhibit diffusion behavior in our tissues and organs as well as self-degradation or cell consumption. As a result, biomolecules are naturally produced and consumed by physical activity again and again (figure 2.1.). Reactive oxygen species (ROS) are metabolites that are produced in cells and play an important role in cell signaling[17, 19]. It has recently become known as an effective biomolecule for regenerative treatment, and it is being used in many studies such as wound healing. As previously stated, ROS is produced spontaneously. Dissolved oxygen in the body receives electrons and conducts an oxidation-reduction reaction, resulting in the formation of numerous types of ROS.

There are occasions where ROS is directly created in biomedical engineering, however I utilized galvanic corrosion via metal potential difference. When two metals with different potentials come into contact, a cathode-anode electrode is created, and ROS is produced by the cathodic metal. ROS measuring technology was required as a basis technology to research the natural generation of ROS and its transfer via artificial generation. There are numerous ways for detecting ROS, including electron spin resonance, electrochemical, and chromatography[20], however the quantity

of ROS required in biomaterials is extremely small, on the order of nanomolar to micromolar.

A chemical ROS quantitative measuring approach using a reagent that can selectively react with ROS was required to measure a tiny quantity. A biodegradable polymeric stent that creates active oxygen is proposed. The previous articles used quantitative analysis to measure three types of ROS. Since there have been research on ROS formation, I thought it would be interesting to investigate the ROS transfer mechanism for direct material application. As a result, H_2O_2 was chosen as a typical ROS for ROS delivery studies. H_2O_2 has all of the properties of a biomolecule and the lowest reactivity among active ROS, therefore it has the fewest side effects in the body, making it the best model molecule for biomaterials. Furthermore, because H_2O_2 is primarily employed for wound healing, fibrin gel, an ECM that plays a crucial role in wound healing, was chosen as the diffusion matrix.

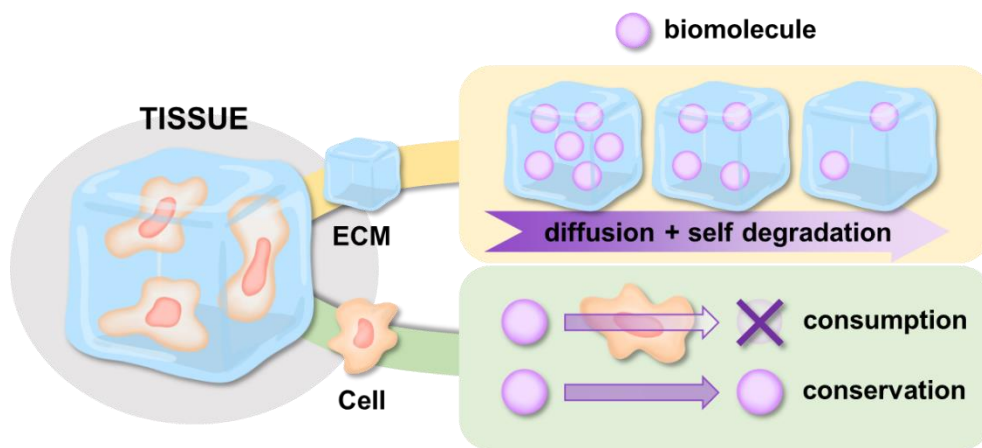


Figure 2.1. Images of self-degradation and cell consumption of H_2O_2 in a tissue that consists of extracellular matrix and cells.

2.2. Experimental Procedures

2.2.1. Kinetics of second order reaction of H₂O₂ degradation

Second-order kinetics provide better fitting findings with H₂O₂ decomposition in fibrin gels. Furthermore, catalytically decomposed H₂O₂ produces hydroxyl (HO·) radicals, which oxidize proteins with second order rate constants, hence the kinetics of second order reaction was used to interpret H₂O₂ degradation in fibrin gel. The kinetics of the second order process are shown below.

$$-\frac{d[C]}{dt} = k[C]^2$$

yields to the following equation.

$$\frac{1}{C} = \frac{1}{C_0} + kt$$

The known data, concentrations (C and C_0), and time (t), were utilized to compute the rate constant by measuring the concentrations in fibrin at each time point (k).

2.2.2. Solution of Fick's second law at constant boundary condition

Fick's second law was used in this study to calculate the diffusion coefficient of H₂O₂ in two concentrations of fibrin gels.

$$\frac{\partial C}{\partial t} = D \frac{\partial^2 C}{\partial x^2}$$

When constant boundary conditions are applied to the preceding equation, the result is:

$$\frac{C(x, t) - C_0}{C_s - C_0} = \text{erfc}\left(\frac{x}{2\sqrt{Dt}}\right)$$

Because of known data, such as concentrations (C and C_0), time (t), and distance of the chip's central channel (x), calculating diffusion coefficient (D) is achievable.

Some decomposition terms caused some variation in Fick's second law. The extinction rate occurs as a multiplied version of Fick's second law solution.

$$C(x, t) = \text{erfc}\left(\frac{x}{2\sqrt{Dt}}\right) \times E(t) \quad Eq(1)$$

Since $C(x, t)$ can be determined experimentally, D may be computed using the equation below from known $C(x, t)$ and $E_{fibrin}(t)$.

$$C(x, t) = \text{erfc}\left(\frac{x}{2\sqrt{Dt}}\right) \times E_{fibrin}(t) \quad Eq(2)$$

$C(x, t)$ in the cell-containing matrix may also be validated experimentally, and $E_{tissue}(t)$ was estimated using the obtained D in the equation above.

$$C(x, t) = \text{erfc}\left(\frac{x}{2\sqrt{D_{2.5}t}}\right) \times E_{tissue}(t) \quad Eq(3)$$

2.2.3. Chip designs and fabrication

Figure 2 depicts the chip creation process. 2. Soft lithography was chosen as a technique for creating lab-on-a-chip devices out of polydimethylsiloxane (PDMS, Sylgard[®] 184, Dow Corning). A photoresist

SU-8 patterned silicon wafer was utilized as a mold, and a degassed PDMS prepolymer mixture (10:1, w/w) was cured on the mold for 2 hours in a 70 °C oven before being peeled away. The PDMS was cut to the desired shape with a blade, and the gel injection pores were punched with a 22-gauge blunt needles, and the reservoirs were pierced with a $\Phi 8$ punch and the right reservoirs with a $\Phi 1$ punch. For one minute, the patterned side of PDMS and one side of cover glasses were O₂ plasma treated at 990V. The plasma-treated PDMS pieces and cover glasses were placed in contact with one another, and adequate pressure was applied to ensure bonding between the PDMS and the glass. The connected lab-on-a-chip devices were placed in a 70 °C oven for 24 to 48 hours to ensure robust covalent bonding between the glass and the elastomer and hydrophobicity recovery.

The chips utilized in this investigation were built with three channels and reservoirs. The width of the chips was 1,000 μm for the left and right channels and 1,300 μm for the center channel, as indicated in figure 2.3. The chips' height and length were also 200 μm and 20 mm, respectively. The chip's reservoirs were adjusted to have different sizes on the left and right sides to meet Fick's second law under constant surface conditions and to improve the efficiency of the H₂O₂ concentration measurement.

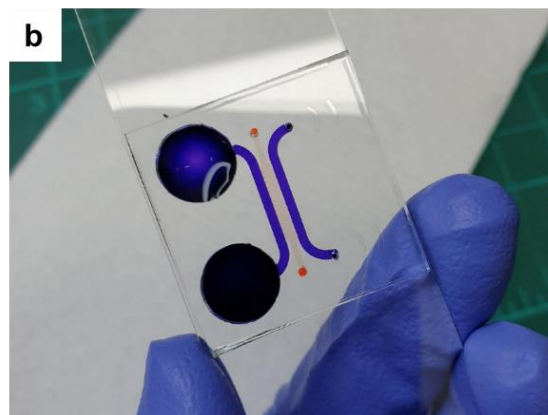
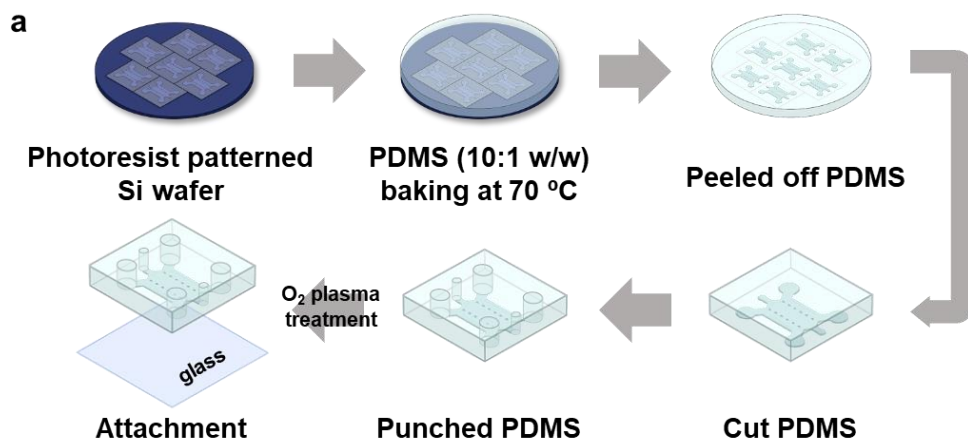


Figure 2.2. (a) The manufacture of microfluidics chips. (b) The produced microfluidics chip used in this investigation, with varying reservoir sizes (8 mm and 1 mm diameter, respectively)

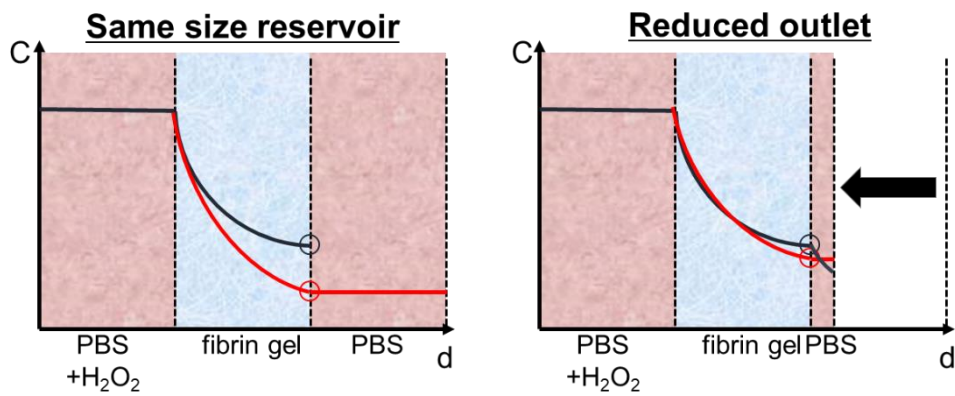
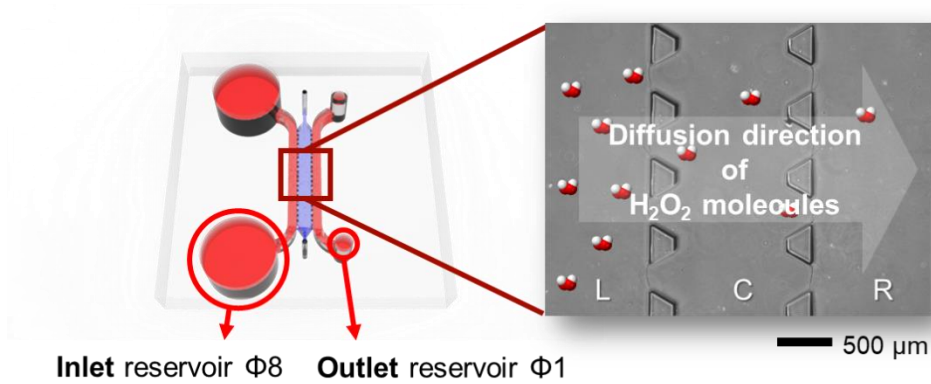


Figure 2.3. An overview of the chip's structure. The diffusion direction changes from left to right channel. The reservoir size was changed to provide for more exact boundary conditions in the solution of Fick's second law.

2.2.4. HUVECs culture

The passage of HUVECs employed in this investigation ranged from 4 to 7. In a petri dish, HUVECs (Lonza) were cultured in endothelial growth medium (EGM-2, Lonza) supplemented with 10% FBS, penicillin (50 U/ml), and streptomycin (50 µg/ml). HUVECs were incubated at 37 °C and 5% CO₂ atmosphere. HUVECs were trypsinized for 3 minutes at room temperature after being washed twice with 1X phosphate buffered saline (PBS). The cell was then trypsin-inhibited with 10 mL of EGM-2. The HUVECs were then centrifuged to eliminate any remaining trypsin from the washing and neutralizing medium. The medium was aspirated except for the cell pellet at the bottom of the centrifuge tube, and the cells were gently resuspended in fresh EGM-2 medium to achieve a 4/3-fold greater cell density (2.66×10^6 cells/ml) than the intended density (2.0×10^6 cells/ml).

2.2.5. Fibrin gel clotting and HUVECs embedding

At 10 mg/ml and 20 mg/ml concentrations, bovine fibrinogen powder (Sigma-Aldrich) was dissolved in 1X PBS (Gibco, with Ca²⁺ and Mg²⁺). A 0.22 µm pored filter was used to filter the bovine fibrinogen solution. The bovine lung aprotinin (Sigma-Aldrich) was then combined with fibrinogen solution (2.0 U/ml). This fibrinogen and aprotinin mixture shall be referred to as fibrinogen mixture from now on. The fibrin concentration at the wound site is estimated to be between 2.0 and 5.0 mg/ml. In this study, two concentrations were chosen that were twice the interval between the two

ranges.

(i) For fibrin gel clotting, the fibrinogen mixture was mixed with PBS in a 1:3 volume ratio, then thrombin (0.08 U/ml) was added. The ultimate concentrations of fibrin gel were roughly 2.5 mg/ml and 5.0 mg/ml, respectively. Because fibrin gel formed in 3 minutes, the pre-crosslinked fibrin was injected into the PDMS chip's middle channel immediately after mixing. The fibrin solution was put in a humidified cell culture incubator for 5 minutes to achieve a full fibrin clot. Following the crosslinking, the rest of the PDMS chips' channels and reservoirs were filled with PBS.

(ii) Resuspended HUVECs in EGM-2 density (2.66×10^6 cells/ml) were prepared for cell embedding in fibrin gel. The fibrinogen mixture was mixed with the resuspended HUVECs in a 1:3 volume ratio, and thrombin was added, as described before (i). After crosslinking, cell medium was put into the chip's left and right channels. When we tested concentrations from the reservoirs three hours after filling, we employed the chip. For morphology study, the cell matrix filled chips were put in a humidified cell culture incubator for 12 hours to allow the cells to stabilize before observing the visible morphological changes. Figure 2.4 depicts injection of both I and (ii).

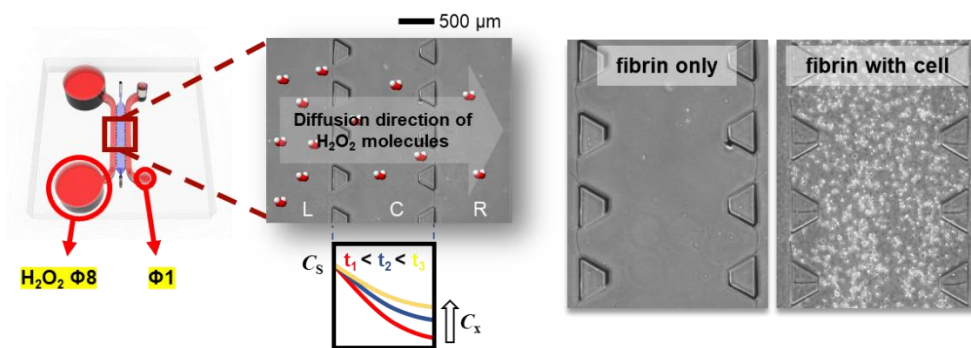


Figure 2.4. Images after fibrin injection into the chip's center channel and fibrin + cell mixture injection into the chip's center channel.

2.2.6. H₂O₂ infusion

Sigma-Aldrich provided a 30% H₂O₂ solution with inhibitor. The solution was diluted to 200 M in PBS and 500 μ M in EGM-2 without vascular endothelial growth factor (VEGF).

(i) For H₂O₂ diffusion coefficient calculations, PBS was removed from both the left and right reservoirs and channels, then refilled with 200 M of H₂O₂ in PBS in the left channels (6 μ l) inlet reservoirs (320 μ l), and only PBS in the right channels (6 μ l) and outlet reservoirs (5 μ l). To eliminate the possibility of interstitial effect affecting diffusion, the volume of H₂O₂ solution and PBS in each reservoir was calculated to have the same height level. Finally, the direction of H₂O₂ diffusion changed from left to right, passing through the center fibrin channel. For each time point, three chips were used.

(ii) For HUVECs with chips, 200 μ M H₂O₂ in PBS was used to compute the sink of the cell containing matrix, which is the same procedure as described before (i). When we studied the reaction of HUVECs, we injected 500 μ M of H₂O₂ solution in EGM-2. Because of its strong growth signaling effects on HUVECs, VEGF was excluded from the HUVECs response study. The right channel was then injected with EGM-2 without VEGF. Also, as previously stated, the same volumes were used for these HUVECs chips.

2.2.7. H₂O₂ concentration measurement

Sigma-Aldrich provided a fluorimetric hydrogen peroxide test kit. H₂O₂ solutions with concentrations of 0, 0.01, 0.1, 1, 5, and 10 μ M were prepared for a standard curve. Because the detection range of fluorescence tagged H₂O₂ concentration is between 0 and 10 μ M, the solutions from the inlet and outlet channels were 25-fold diluted for measurements, taking the original concentration of H₂O₂ and the inlet into account. The kit was used to add 50 μ l of fluorescence tagging markers to 50 μ l of diluted H₂O₂ solutions. After 20 minutes, the fluorescence tagged H₂O₂ solutions were read with a fluorescence plate reader (GloMax) at wavelengths of $\lambda_{\text{ex}} = 540$ and $\lambda_{\text{em}} = 590$ nm. The concentrations of H₂O₂ were calculated by multiplying the fluorescence intensity from the inlet and outlet solutions by a factor of 25 and comparing it to the fluorescence intensity from the H₂O₂ standard curve.

2.2.8. H₂O₂ degradation measurement

In fibrin gel, the rate of H₂O₂ breakdown was assessed. With 10 μ M H₂O₂, fibrin gels of 2.5 and 5.0 mg/mL were created. H₂O₂ was detected at each time point using a fluorescence indicator, as described in section 2.2.7. For 3 hours, the concentration was measured every 30 minutes with a fluorescence plate reader at $\lambda_{\text{ex}} = 540$ and $\lambda_{\text{em}} = 590$ nm.

2.2.9. Immunostaining

The collagen was made in the same manner as previously reported.

An amine labeling dye, 0.1% volume of Alexa Fluor® 555 NHS Ester, was added to the entire volume of the collagen mixture solution for imaging. The collagen solution containing color was properly blended. Non-binding dyes were rinsed with PBS after the same gelation method was performed on the chip.

2.3. Results and Discussion

2.3.1 Fibrin matrix characterization

The colored fibrin matrix was photographed as well as colored. Figure 2.5 shows that the density of the mesh differed between two concentrations (2.5 and 5.0 mg/mL), and the percentage area of the fibrin fibers differed statistically. Because H_2O_2 is such a small molecule, there would be no critical barriers to H_2O_2 diffusion in both concentrations of fibrin gel.

2.3.2 Self-degradation of H_2O_2

H_2O_2 self-degradation measurements were fitted to 2nd order kinetics. Because the concentration was measured at 30-minute intervals for 3 hours, this is enough data for fitting. Normalized to 1.0, the starting concentration was given as a decomposition rate. As a result, H_2O_2 was reduced by 0.8 times and 0.6 times the initial concentration in 2.5 mg/mL and 5.0 mg/mL fibrin gel, respectively, after 3 hours. With the passage of time, it was established that H_2O_2 went through a self-degradation process within the fibrin, which is thought to be a phenomenon that occurs concurrently when H_2O_2 is transported from the fibrin gel.

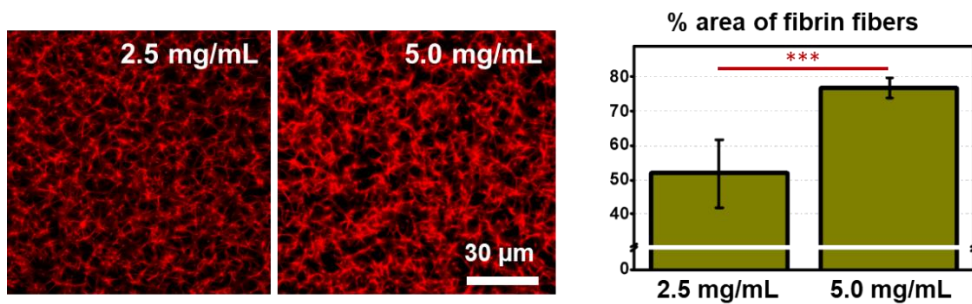


Figure 2.5. Dyed pictures of two fibrin concentrations, 2.5 and 5.0 mg/ml, used to compute the diffusion coefficient and self-decomposition rate of H_2O_2 . ImageJ was used to calculate the percentage area of fibrin fibers. (** $p < 0.001$)

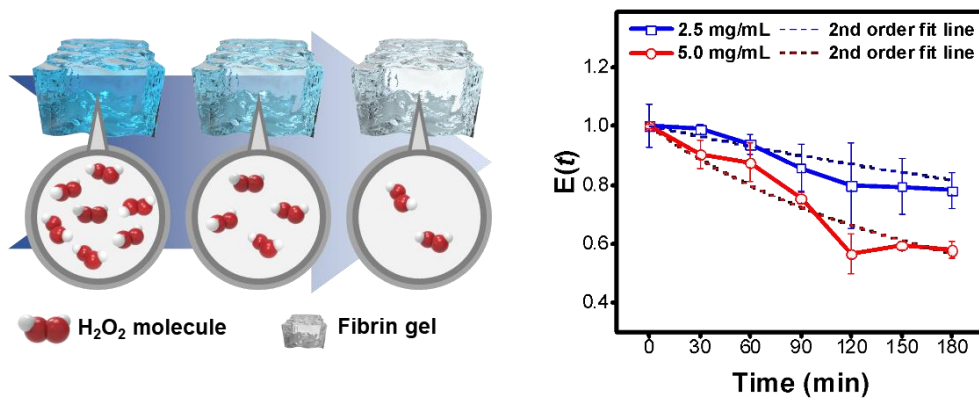


Figure 2.6. The degradation of H_2O_2 in fibrin gel is seen schematically on the left. The rate of H_2O_2 decomposition was monitored at 30-minute intervals and is graphed on the right. The graph illustrates that a higher fibrin concentration of 5.0 mg/mL results in a faster degradation rate.

2.3.3. H₂O₂ diffusion coefficient (D)

By measuring the H₂O₂ concentration at 2.5 and 5.0 mg/mL of fibrin, the diffusion coefficient was determined (Fig. 2.7.). The concentration of H₂O₂ measured at 5.0 mg/mL is substantially lower than that recorded at 2.5 mg/mL. We could calculate the diffusion coefficient in 2.5mg/mL fibrin ($D_{2.5}$) and 5.0 mg/mL fibrin ($D_{5.0}$) using eq (2) with the value of $E_{fibrin}(t)$ and experimentally verified $C(x, t)$. $D_{2.5}$ has a value of $2.62 \times 10^{-10} \text{ m}^2/\text{s}$, whereas $D_{5.0}$ also has a value of $1.33 \times 10^{-10} \text{ m}^2/\text{s}$. The diffusion coefficient was likewise lowered by half when the fibrin concentration increased twice. The spatiotemporal distribution of ROS may be predicted using the diffusion coefficient, and the degree of diffusion in active oxygen releasing implants can be measured.

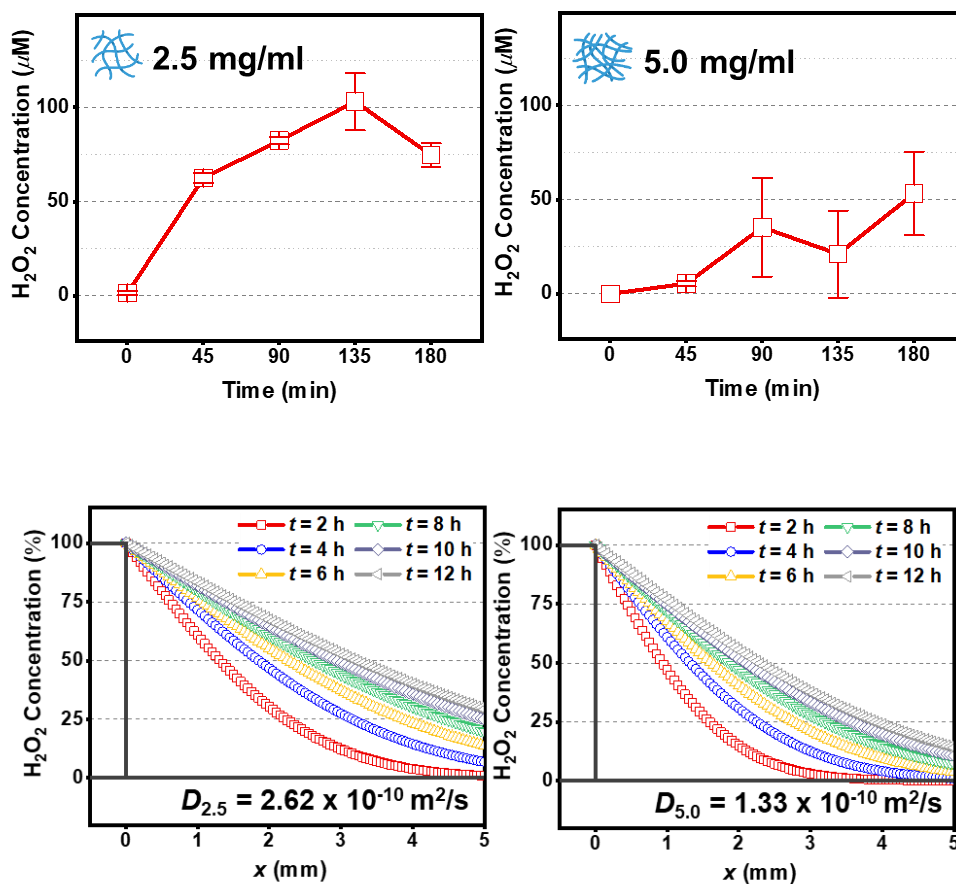


Figure 2.7. H₂O₂ concentration after diffusion and concentration patterns in two types of gels were measured. The concentration of fibrin from the output reservoir was monitored every 45 minutes for 3 hours at 2.5 mg/mL and 5.0 mg/mL. $C(x, t)$ values were shown below the concentration graphs using the calculated D .

2.3.4. H₂O₂ Consumption by cells

The same experiment was carried out on the microfluidics chip, but this time the matrix comprised HUVECS. HUVECs are known to be extremely resistant to H₂O₂. As a result of the high H₂O₂ consumption, it is predicted that the concentration of H₂O₂ measured in the output reservoir will be substantially lower since the H₂O₂ is consumed in the HUVEC-containing fibrin.

Fig. 2.8. The concentration of H₂O₂ recorded per hour at the outflow reservoir was substantially lower than the concentration depicted in Figure 2.7, as predicted. Based on the equation below, not only the extinction rate of tissue ($E_{tissue}(t)$), but also the extinction rate of HUVEC and fibrin ($E_{HUVEC}(t)$ and $E_{fibrin}(t)$) were computed.

$$(1 - E_{HUVEC}(t)) + (1 - E_{fibrin}(t)) = (1 - E_{tissue}(t))$$

According to the experimental data, degradation in fibrin itself appears to diminish over time, whereas the effect of consumption by cells steadily rises. Based on this, the spatiotemporal distribution (figure 2.9.) may be predicted by displaying the profile of how H₂O₂ diffuses in the real tissue, passing through self-degradation and consumption, and at what concentration it is transported.

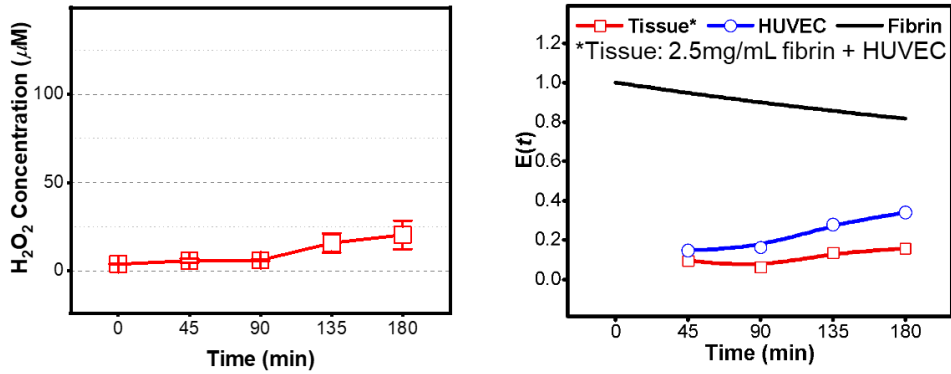


Figure 2.8. (Left) Fibrin concentration detected in cell outflow reservoir. (Right) The extinction rates of HUVEC and fibrin itself can be calculated from the extinction rates of tissue. The cell-containing matrices (tissue and HUVEC) were treated as meaningless when the value at $t = 0$ was stated.

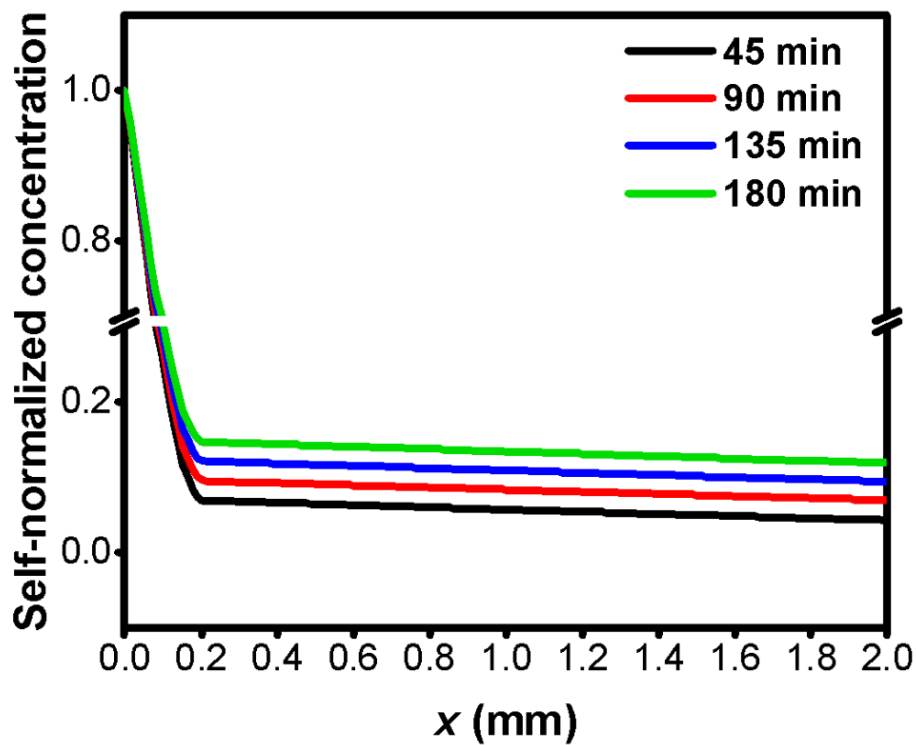


Figure 2.9. H₂O₂ distribution in cell-containing tissue over 45, 90, 135, and 180 minutes. When compared to the initial concentration, the concentration at $x = 2.0$ mm is less than 20%.

2.3.5 Cell response against H₂O₂ gradient

Rather of just displaying the profile, experiments on how real cells react were carried out. When the chip area's central channel was separated into three portions, the control group (no H₂O₂) displays equally scattered green-stained cells, indicating that the live cells were well distributed inside the channel (figure 2.10.). However, testing settings with an H₂O₂ gradient revealed that section 3 had more viable cells than section 1. When the cells inside the matrix are stained at a higher magnification, many cells fail to extend actin in section 1, whereas section 3 reveals the early stage in which HUVECs stretch actin and assemble to create blood vessels. Overall, the vascular cells in section 1 were strongly influenced by high H₂O₂ concentrations and were unhealthy, but the concentration of H₂O₂ was low in section 3, indicating a tendency toward healthy cells.

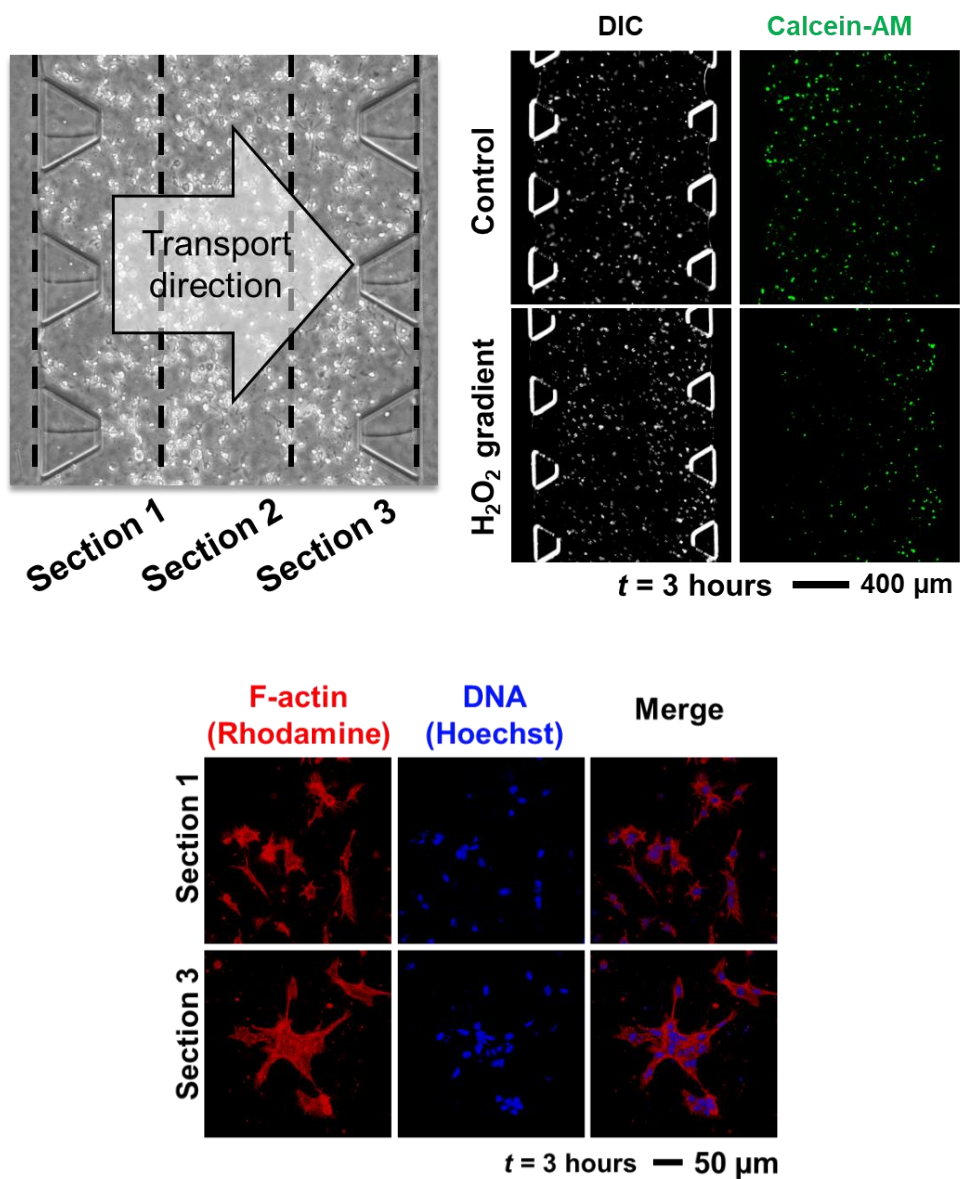


Figure 2.10. The HUVEC reaction to the H_2O_2 gradient in the matrix. When the region was partitioned into three pieces, the cell response differed when an H_2O_2 gradient was established. HUVECs in section 1 tend to show apoptosis three hours after being injected with 200 μM of H_2O_2 , whereas HUVECs in section 3 prefer to aggregate to form vessels.

2.4. Conclusion

To summarize, the self-degradation rate of H_2O_2 and D value of H_2O_2 at two fibrin concentrations were computed. This platform was used to predict both diffusion and sink based on those parameters. As a consequence, we knew how H_2O_2 is distributed in space and time, and we validated that the cellular reactivity has the same tendency as a result of modeling via studies.

One constraint of this work is that, while modeling is simple, there is a methodological complication in measuring concentration at each time point. Furthermore, utilizing a static chip to maintain the boundary condition is not ideal, and the target region is obscured, with just the transfer of H_2O_2 known.

Despite these constraints, this investigation enabled me to mimic and comprehend the transport mechanism that reflected material properties/confirmed that cells were geographically differently impacted. This platform is projected to make it much easier to mimic generic nutrients or proteins with less self-degradation in materials. With the cell test, I just evaluated viability, but more relevant tests may be created using a wider range of cells and materials.

Chapter 3. Diffusion of Nanocarriers

3.1. Introduction

Substance transport is a key phenomenon in the maintenance of life. A quantitative knowledge of transport is required for biological studies on nutrition and waste movement, medication and protein delivery for cancer therapy, and tissue regeneration[9, 21]. The principal transportation method in our body is convective flow through the bloodstream, and at the final stage, various types of molecules flow out of the vessel walls and display diffusive transport behavior across the extracellular matrix (ECM) to the cells consuming them[14, 22-24]. Some research focus on movement or diffusion since it is crucial to comprehend how it functions in the ECM[25-27]. As a result, the diffusivity of molecules of interest must be determined in order to examine specific biological events in the body, notably in drug delivery studies in which injected medications flow with the blood, travel out through the channel, and diffuse to the target cells at the end[28]. As a result, in order to estimate the duration of action of pharmaceuticals and their ideal dosages, the diffusion behavior of drug molecules or drug carriers must be quantitatively explained.

To date, cell tests followed by animal tests have been used to evaluate the pharmaceutical efficacies and safety issues of candidate drug compounds; however, only a few (5%) of the over 400,000 drug candidates that passed *in vitro* tests were successful in animal tests[29], resulting in a massive waste of

time, animal and human resources, and research funds. This is mostly due to a disparity between *in vitro* cell testing and *in vivo* animal experiments. Cells in conventional *in vitro* experiments are incubated in a homogeneous liquid under static 2-dimensional (2D) conditions with no major diffusive processes, whereas cells in living animals lie in 3-dimensional (3D) heterogeneous and condensed phases under dynamic conditions with the diffusion mechanism prevailing during material transport[30]. To bridge the gap between *in vitro* cell testing and *in vivo* research, it is critical to create approaches that give a quantitative knowledge of drug or carrier diffusional characteristics under dynamic settings in the condensed phase, which is similar to the *in vivo* system.

Microfluidics chips provide the best *in vitro* platform for diffusion modeling investigations that mimic *in vivo* settings[3, 31, 32]. Dynamic flow[33-35] and 3D cell culture utilizing ECMs[2, 36-38] may be implemented using microfluidic chips. Because the concentration of substances can be easily controlled channel by channel during diffusion experiments and nearly ideal boundary conditions can be maintained, the spatiotemporal transport behavior of drugs or drug carriers can be estimated by fitting concentration data to the diffusion equation.

Based on chips and fluorescence diffusivity investigations, we present a simple approach for evaluating the diffusivity of drug carriers in this paper (figure 3.1.). We utilized biocompatible mesoporous silica nanoparticles (MSNs) as model molecules since there have been numerous

research on them due to their growing relevance in therapeutic and diagnostic applications. They have the advantage of being able to function independently or as carriers for other molecules like as proteins[39, 40], drugs[41-43], or RNAs[44, 45] because of their unique qualities such as ultrahigh specific surface area, ease of surface modification, customizable particle size, and great biocompatibility. Furthermore, the MSN is deemed by the US Food and Drug Administration[46-48] to be widely recognized as safe amorphous silica, which is a significant advantage for the carrier. We chose collagen as a diffusion matrix because most drug delivery research is focused on cancer tissues, where collagen is the main ECM. We chose collagen as a diffusion matrix because most drug delivery research is focused on cancer tissues, where collagen is the main ECM[37].

Collagen is the most fundamental and multifunctional matrix for tumor research because physical and chemical properties of collagen, such as density, alignment, or binding site, impact cancer cells[37, 49, 50]. In addition, collagen is an ideal matrix for three-dimensional cell growth in a laboratory setting. For these reasons, collagen-containing matrices are used in conjunction with other composites to research tumors and their microenvironment. Because of these applicable features and the importance of understanding nanoparticles, an increasing number of research studies reveal the significance of nanoparticle transportation in collagen-containing ECM such as a mix with fibrin or any other hydrogels in that ECM can operate as a wall or filtrate compounds or nanomaterials[51-54].

We also employed chip devices with three channels: one in the middle filled with collagen and two on the sides to simulate the bloodstream. To promote MSN diffusion in collagen, a solution containing fluorescence-tagged MSNs was injected into a channel. Following that, we calculated the diffusivity of MSNs and predicted their spatiotemporal distribution in collagen by evaluating the fluorescence profile in collagen at a specific time point and fitting it to the diffusion equation, thereby mimicking the behavior of nanocarriers passed through the blood vessel to the ECM in tissues.

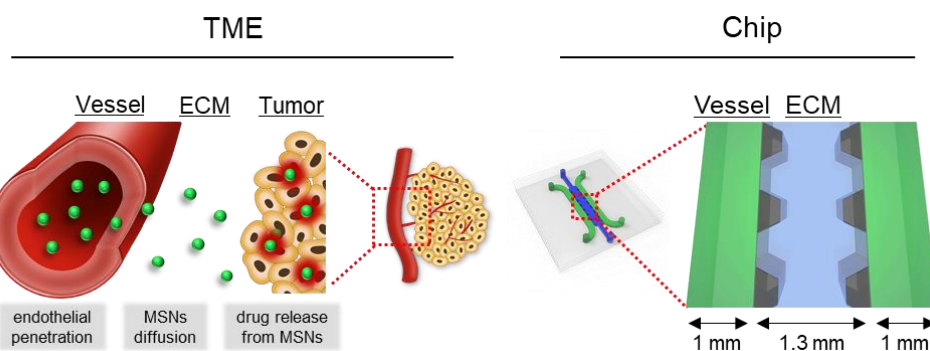


Figure 3.1. The tumor microenvironment and microfluidics chips are depicted schematically. The blood vessel and ECM in the left image correspond to the same portion of the chip as seen in the right image.

3.2. Experimental Procedures

3.2.1. Materials

Sigma-Aldrich, USA, provided the cetyltrimethylammonium bromide (CTAB), tetramethylorthosilicate (TMOS), tetraethyl orthosilicate (TEOS), triethanolamine (TEA), N-hydroxysuccinimide (NHS), and 1-Ethyl-3-(3-dimethylaminopropyl)-carbodiimide (EDC). NHS-fluorescein (5-(and 6-)carboxyfluorescein, FAM) was obtained from Thermo Fisher Scientific in the United States. Dow Corning, USA, supplied SYLGARD[®] 184 for chip manufacturing. Sigma-Aldrich in the United States provided dopamine hydrochloride for polydopamine coating. Corning, USA, provided collagen type I from rat tail in acid. Thermo Fisher Scientific supplied the Alexa Fluor[®] 555 NHS ester for collagen labeling[55].

3.2.2 Preparation of MSNs

MSNs were created using a modified sol-gel approach previously described[10, 56]. As a control for pH settings for a suitable catalytic reaction, CTAB with TMOS or TEOS was utilized. CTAB (83.8 mg) and TMOS (0.096 mL) were reacted at room temperature in an ammonium hydroxide/ethanol solution to produce 10 nm particles. At 40 °C, MSNs with a particle size of 45 nm were produced in a TEA (0.028 g) solution containing CTAB (0.33 g) and TEOS (0.73 mL). CTAB (4.16 g) and TEOS (0.36 mL) were treated in ammonium hydroxide/methanol solution at 30 °C to produce 100-nm MSNs.

At room temperature, TMOS (1.3 mL) was added to CTAB (4 g) and dissolved sodium hydroxide/methanol solution to generate 200-nm, 500-nm, and 1- μ m sized MSNs. The methanol/water molar ratios in this process were 1:2.26, 1:1.7, and 1:1. The collected materials were calcined in a furnace for 4 hours at 550 °C to eliminate the template CTAB. Finally, FAM-tagged MSNs were created by performing an NHS/EDC reaction between MSNs and NHS-fluorescein[55].

3.2.3 Measurement of Raman Spectra

Drop-casting, a simple, quick deposition process performed at room temperature, was used to deposit the MSNs onto the SiO₂ substrate. The Raman spectra were captured using an InVia Raman Microscope (Renishaw, UK), model $\times 50$, with a 532 nm laser at 10% power and a 10 s exposure duration.

3.2.4 Chip Fabrication

The chip was meant to imitate a mechanism in which nanoparticles were carried to the tumor. The diffusion coefficient is computed using a three-channel chip. To create a polydimethylsiloxane (PDMS) lab-on-a-chip, silicone elastomer and curing agent were combined in a 10:1 (w/w) ratio and poured into an SU-8 patterned silicon mold. Degassing is required before hardening into intricate designs. The degassed PDMS mixture on silicon mold was then baked in a 70 °C oven for 2 hours. The peeling PDMS was sliced

and punctured as needed. The PDMS pieces were mounted to the cover glasses using O₂ plasma surface treatment, then baked in a 70 °C oven overnight to eliminate surface radicals. The entire sample was rinsed with ethanol, then with distilled water.

3.2.5 Channel Coatings

Before perfusion, the MSN perfuse channel was surface treated for 1 hour with 10% (v/v) TEOS in ethanol to avoid particle aggregation inside the channel[57], particularly at the top and bottom, and the TEOS residue was rinsed with ethanol twice and dried naturally. The collagen injection channel was coated with polydopamine (PDA) after TEOS coating to increase collagen adherence to the channel surface[58, 59]. Dopamine hydrochloride working solution (2.0 mg/mL) was produced in distilled water with 10 mM Tris-HCl. The dopamine working solution was vortexed sufficiently before being put into the chip's central channel and left to coat at room temperature. The dark-colored solution was rinsed twice with distilled water and dried naturally after 2 hours.

3.2.6 Collagen Preparation and Gel Insertion

For this study, a high concentration (10 mg/mL) of collagen type I from rat tail in acid was adopted. The original stock collagen solution was diluted with 10 PBS, 1 N NaOH, and distilled water to yield 2.0 mg/mL (0.2%) collagen matrix. The components used in each phase were put in an ice bucket

before gelation. The mixed solution was injected into the chip's central channel and incubated for 10 minutes in a humidified incubator at 37 °C. To prevent the matrix from drying out after full gelation, the peripheral channels were filled with 1× PBS solution.

3.2.7 Connection of LOC to the Syringe Pump

MSN solutions were pre-sonicated and linked in a Tygon[®] tube (USA, ID 0.020/OD 0.060 in.). The opposite end of the tubing was attached to each of the chip's perfusion inlets. Syringes were loaded into an infusible syringe pump (Harvard Apparatus, USA) and securely fixed to prevent movement during infusion. The left channel corresponds to MSN perfusion at 50 µg/mL, whereas the right channel corresponds to PBS perfusion. Given the size of the infusion channel, the flow rate was set at 450 µL/h, which was translated to 625 µm/s[31, 60]. For 3 hours, the syringe pump-connected LOC was put in a humidified incubator at 37 °C.

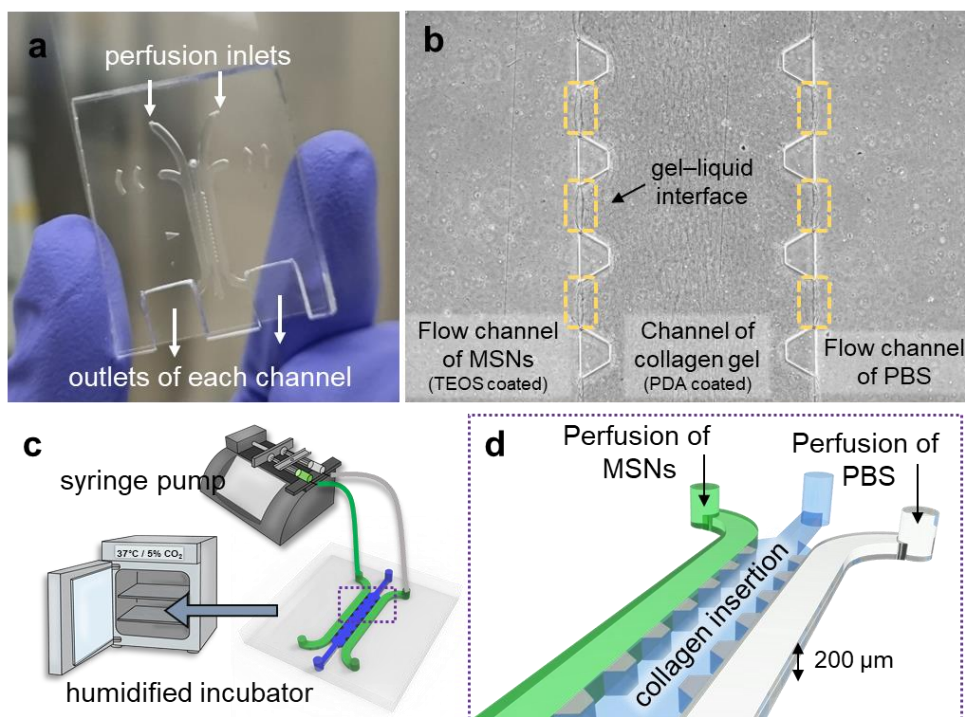


Figure 3.2. (a) An example of a perfusion chip with inlets and outputs. On, an optical picture of the chip's inside is taken (b). After injecting collagen gel and PBS into peripheral channels, the gel-liquid interface (yellow dotted box) developed. TEOS and PDA were used to coat the left and center channels, respectively. (c) The connection between the syringe pump and the gel-injected microfluidics chips. During the perfusion, the chips were put in a humidified incubator for 3 hours. 3D representation of the chip is presented on (d).

3.2.8 Collagen Dying and Mesh Imaging

The collagen was made in the same manner as previously reported. An amine labeling dye, 0.1% volume of Alexa Fluor[®] 555 NHS Ester, was added to the total volume of the collagen mixture solution for imaging of the collagen mesh. The collagen solution containing color was properly blended. Non-binding dyes were rinsed with PBS after the same gelation method was performed on the chip. The mesh pictures were acquired at low and high magnifications using a confocal microscope (LSM 700, Zeiss, Germany). In addition, by recording 454 sliced photos from bottom to top, a 100-μm height 3D stacked image was created. For sample scanning, a laser with a wavelength of 555 nm was utilized.

3.2.9 Image Analysis

ImageJ software was used to measure the sizes of nanoparticles (NIH, USA). ImageJ was used to gather at least four particle diameters in each image by measuring the length of the straight lines across the particles. The data was then averaged and displayed. The fluorescence profile in the central channel filled with collagen (width: 1,000 μm) was collected and analyzed using ImageJ software for diffusion modeling. The pictures of the center channel were trimmed to a size of $1.0 \times 0.3 \text{ mm}^2$ and each image was divided into red, green, and blue channels. Following that, just the green channels were studied, and the intensity values at location x in the rectangle pictures were averaged. The green channel picture profile was transformed to

grayscale, and pixels were converted to real distance. The original intensity was supposed to be in the upper left corner of the picture. The gradients were fitted using MATLAB (MathWorks, USA) using the diffusion model outlined below to get the diffusion coefficient after the starting intensities were normalized to 100%.

3.2.10 Diffusion Model

Fick's second law was used to calculate the diffusion coefficient (D) of MSNs in the collagen matrix. In terms of drug administration, the surface concentration of nanoparticles at the lesion (C_s at $x = 0$) and the bulk concentration in the blood (C_0 at $x = \infty$) were considered to remain constant.

$$\frac{\partial C}{\partial t} = D \frac{\partial^2 C}{\partial x^2}$$

For $t = 0$, $C = C_0$ at $0 \leq x \leq \infty$

For $t > 0$, $C = C_s$ (the constant surface concentration) at $x = 0$

$$C = C_0 \text{ at } x = \infty$$

Setting the limit by using concentration boundary conditions in our experiments offers the answer to Fick's second law:

$$\frac{C_x - C_0}{C_s - C_0} = \text{erfc}\left(\frac{x}{2\sqrt{Dt}}\right) = 1 - \text{erf}\left(\frac{x}{2\sqrt{Dt}}\right) \quad eq(1)$$

where C_x represents the nanoparticle concentration after time t at distance x from the sol-gel interface. The surface and bulk concentrations were $C_s = 100 \mu\text{M}$ and $C_0 = 0 \mu\text{M}$, respectively, and the fluorescence

concentration of MSNs was monitored at $x = 0$ to 0.001 m for $t = 10,800$ s. The diffusion coefficients for different particle sizes ranging from 45 nm to 1 μm are given by a least-squares fit of the complementary error function to the concentration data; the curve-fitting method produces an appropriate estimate by finding the minimum of the unconstrained multivariable function, $C(t) - (1 - \text{erf}(\frac{x}{2\sqrt{Dt}}))$, using a derivative-free method.

3.2.11 Statistics

All data were combined and given as mean \pm standard error (SE). In the study, three or more independent pictures were employed. One-way ANOVA was used to establish statistical significance, followed by Tukey's post hoc test. $^*p < 0.05$ and $^{***}p < 0.001$ were considered to be significant ($^{**}p < 0.01$ was excluded because a significance level of 0.01 is included in that at 0.001). The tests were carried out utilizing the OriginPro 9.0 program (OriginLab Corporation, USA).

3.3. Results and Discussion

3.3.1 Characterization and preparation of MSNs

Because the level of renal clearance, liver capture, splenic filtration, interendothelial cell slits, and lung accumulation of materials are greatly dependent on molecule size, carrier size is an essential characteristic that may be measured in vivo by their distribution and behaviors[61-63]. To explore the mobility of nanoparticles in the ECM, we first produced MSNs of various sizes as possible drug carriers. Figure 3.3 depicts transmission electron microscopy (TEM) pictures of MSNs with particle sizes of 10, 45, 100, 200, and 500 nm and 1 μm . Figure 3.4(a). depicts the average particle sizes of MSNs determined using Image J program from three to five photos. Nitrogen sorption studies indicated that the produced MSNs had a pore size of 3.03 ± 0.14 nm, a pore volume of 3.09 ± 0.19 cc/g, and a huge surface area of $1,934 \pm 16.52$ m²/g, allowing pharmaceuticals to be loaded into the pores³ (Figure 3.4(b).). All particles had a negative surface potential of 21.58 ± 20.94 mV due to a SiOH surface group (Figure 3.4(c).).

Following that, we created fluorescent MSNs for optical imaging-based particle transportation investigation in the LOC system. A standard curve of fluorescence intensity was established by mixing the same fluorescent dye per particle to minimize the analytical error generated by fluorescence measurement (Figure 3.4(d).). These findings show that MSNs were effectively produced and that the study may now focus entirely on MSN

particle size.

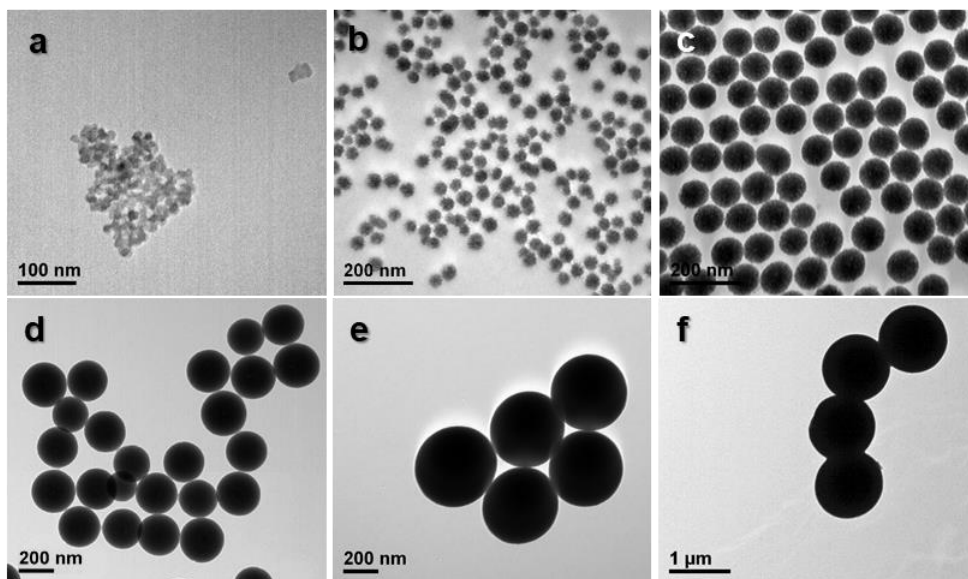


Figure 3.3. The TEM images of MSNs. The diameters are 10 nm (a), 45 nm (b), 100 nm (c), 200 nm (d), 500 nm (e), and 1 μ m (f), respectively.

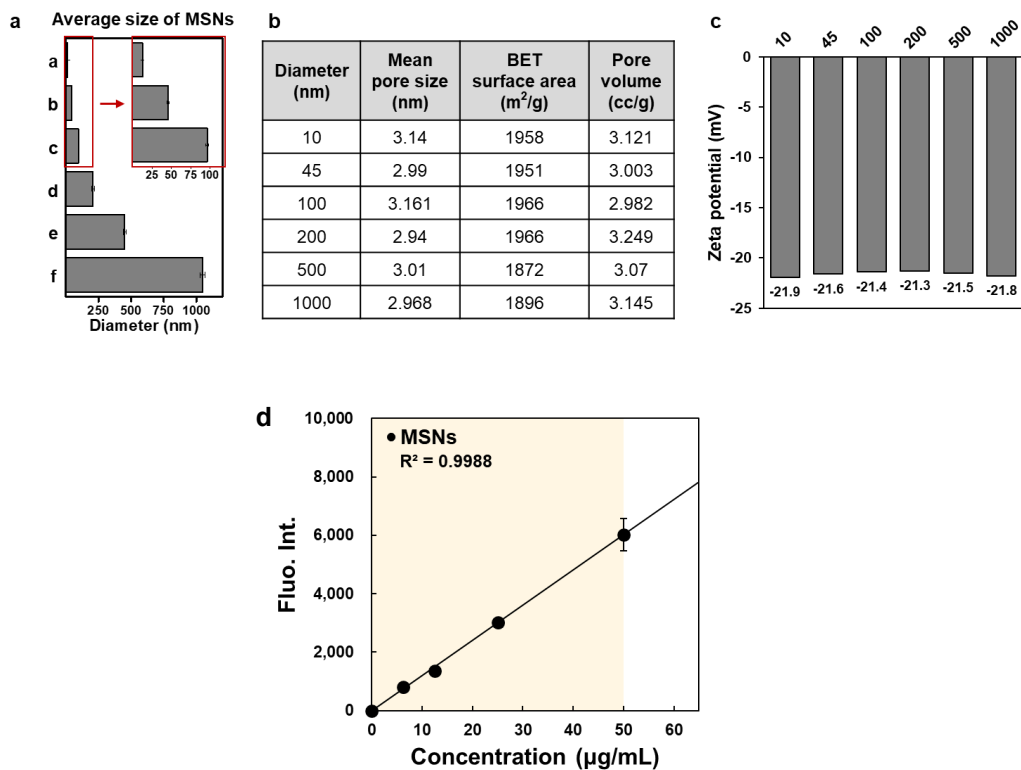


Figure 3.4. (a) Based on the images, the average particle size was also obtained. (b) In addition, the physical properties of each particle are displayed in. (c) The particles' zeta potential was also measured. (d) MSN fluorescence intensity was also measured.

3.3.2 Confirmation of diffusion capability of MSNs in collagen matrix

We created a 0.2% (w/v) collagen matrix to study the diffusion of MSNs in the tumor microenvironment since collagen is the most common ECM in the body and tumor tissue (TME). Fluorescence imaging of the 3D fiber structure of the collagen gel dyed with Alexa Fluor[®] 555 validated mesh size (10 μm) and matrix homogeneity (figure 3.5.). If the collagen mesh is the same size as or smaller than the nanoparticles, it can act as a barrier to MSN transport through the matrix. Because the collagen mesh size of about 10 μm was significantly bigger than the biggest MSN (1 μm) employed in this work, MSNs of any size could easily travel inside the collagen matrix. Furthermore, the collagen put into the channel was distributed uniformly (Figure 3.5.(c)) across the channel. The PDA coating accomplished this uniformity by allowing collagen to adhere to the surface of the PDA-coated PDMS (figure 3.6.). Overall, based on the collagen matrix structures, it can be concluded that the produced collagen is an appropriate medium for studying the transportation behavior of MSNs up to 1 μm in size with only one dominant variable, that is, the size of the MSNs.

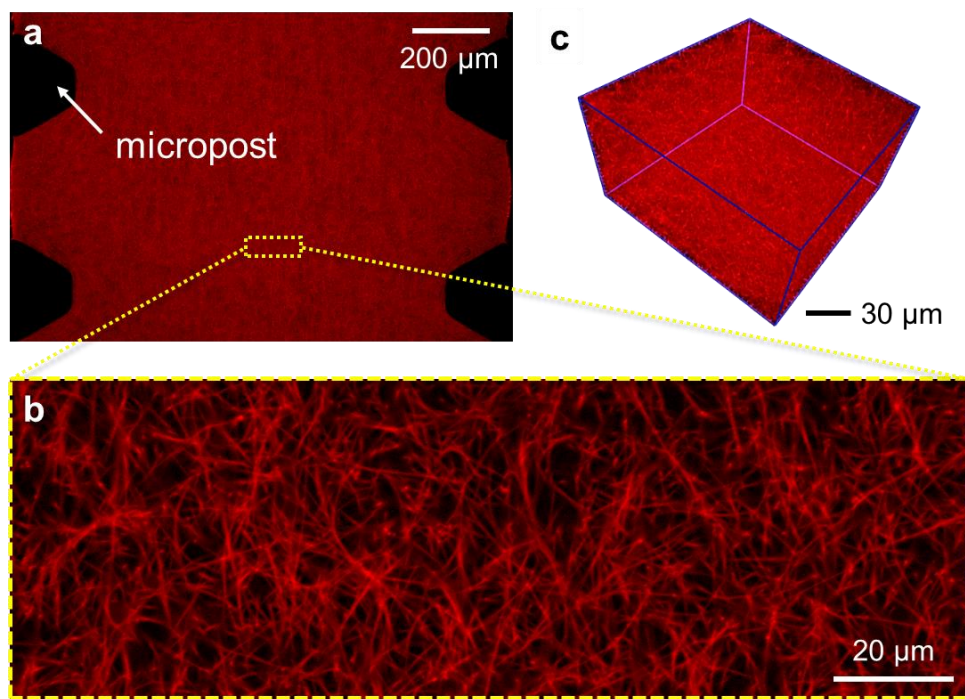


Figure 3.5. 0.2% collagen mesh and homogeneity. (a) Injected collagen (0.2%) into the chip's central channel. Alexa Fluor[®] 555 NHS Ester (ex: 555 nm/em: 572 nm) was used to stain the collagen fiber. (b) A greater magnification picture of collagen fibers. The collagen mesh size appears to be 10 μm. (c) The 3D fiber structure of homogenous collagen gel was detected using z-stacking.

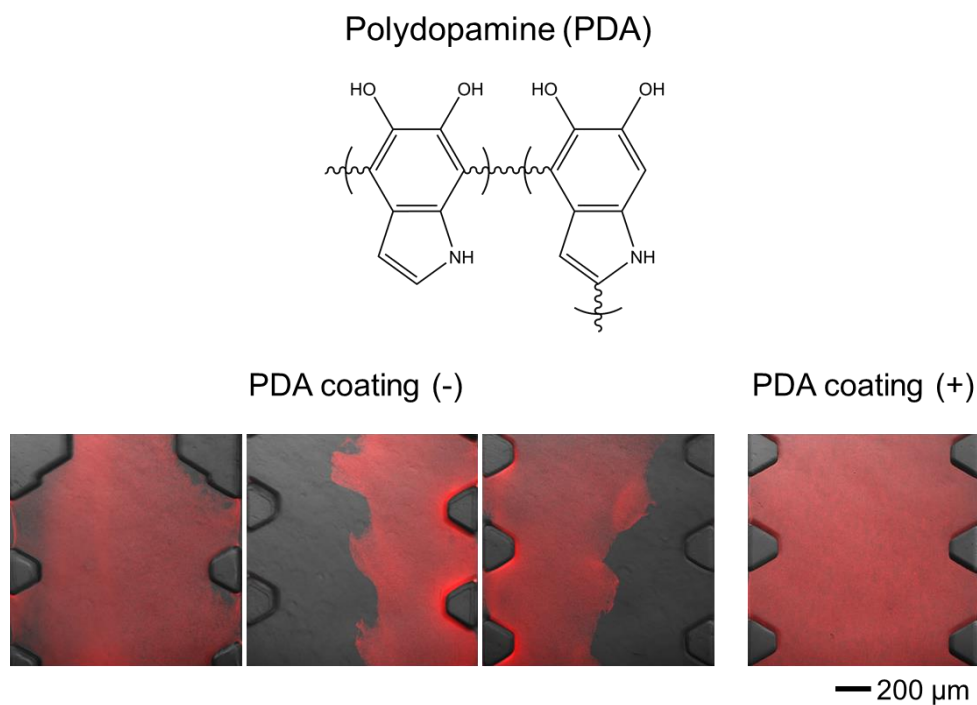


Figure 3.6. The chemical structure of polydopamine (PDA), as well as the non-coated and coated polydopamine channels. Due to PDA shrinking issues, collagen was detached from the channel if the PDA coating was not done in the channel. The collagen structure was physically preserved when the PDA coating was applied.

3.3.3 Experimental realization of boundary conditions and acquisition of concentration gradient data

Using PDMS, we created a perfusable three-channel microfluidic chip. Each channel, as illustrated in figure 3.7, is separated into microposts, allowing MSNs in the side channel to flow into the collagen between the microposts. PBS containing 50 $\mu\text{g/mL}$ MSNs (C_s in equation (1)) was perfused in the left channel, whereas only PBS without MSNs was perfused in the right channel to set the boundary conditions ($C_o = 0$). To avoid MSN aggregation and maintain a steady concentration, TEOS was coated on the left channel, and it can be seen that the TEOS coating significantly reduced MSN aggregation in the channel (figure 3.8.).

Meanwhile, collagen produces contraction issues during gelation, particularly at the interface between collagen and MSN-containing PBS, which is where MSN diffusion begins. To reduce contraction-related issues at the gel-liquid interface and collagen detachment from the surface, PDA was coated inside the central channel[41, 59], which reduced significant collagen detachment or inhomogeneity. Nonetheless, because of collagen contraction during the gelation process while maintaining PDMS microposts wetting, the geometry of the gel-liquid interface varied from a straight line, as well as using interface pictures for analysis may result in insufficiency due to inaccurate fluorescence information. As a result, we used the center channel cut image with an area of $1.0 \text{ mm} \times 0.30 \text{ mm}$. MSNs move through the collagen gel from the left to the right channel as MSN-containing PBS is

perfused on both the left and right channels at the same time. As a result, a concentration gradient forms in the gel (figure 3.9., after 3 h perfusion), and the diffusion coefficient (D) of MSNs in collagen can only be estimated by recording and fitting the fluorescence profile indicating the concentration gradient to the mathematical solution.

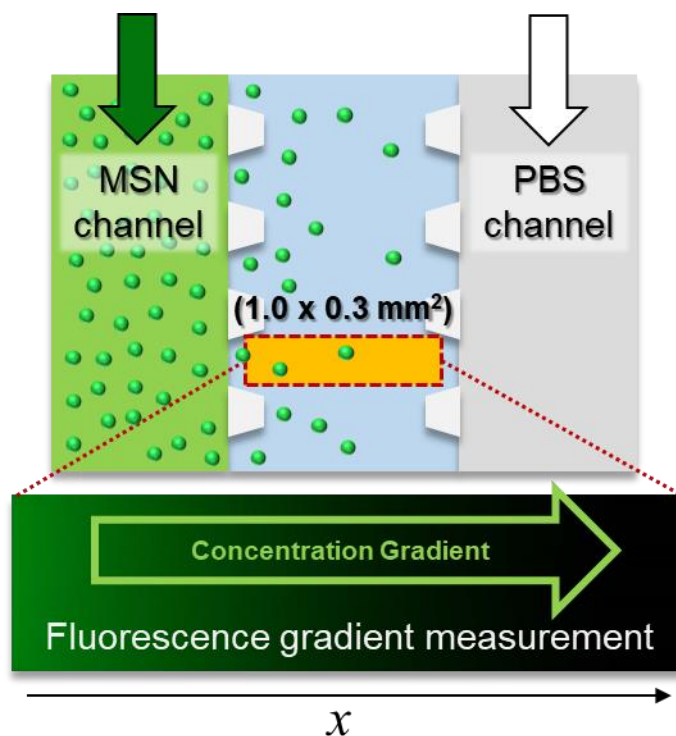


Figure 3.7. MSNs diffuse in the chip's collagen matrix. Schematic of induced diffusion in the chip. MSN diffusion coefficients were calculated using the square boxed region. Fluorescence-tagged particles moved at a steady rate in the left channel, whereas particle-free PBS moved at the same rate in the right.

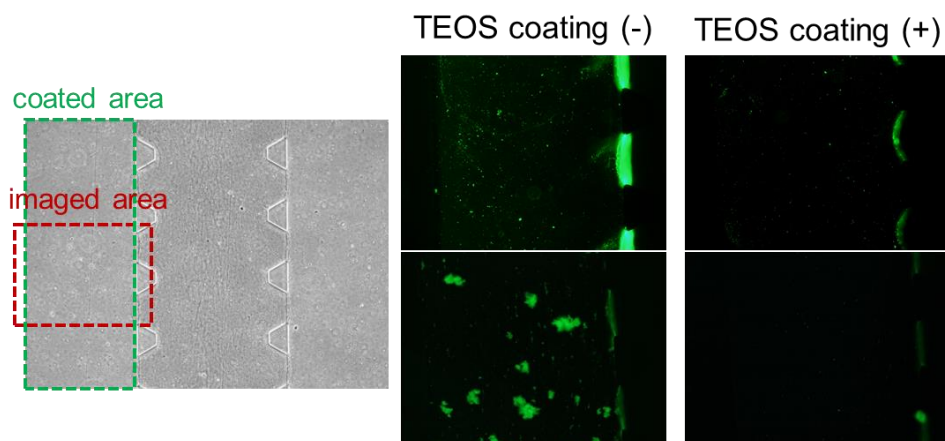


Figure 3.8. To prevent MSN aggregation, TEOS coating was applied within the left channel. Without the coating method. MSNs clustered together, making it difficult to obtain distinct diffusion pictures. However, because there was no aggregation with TEOS coating, clear data were obtained.

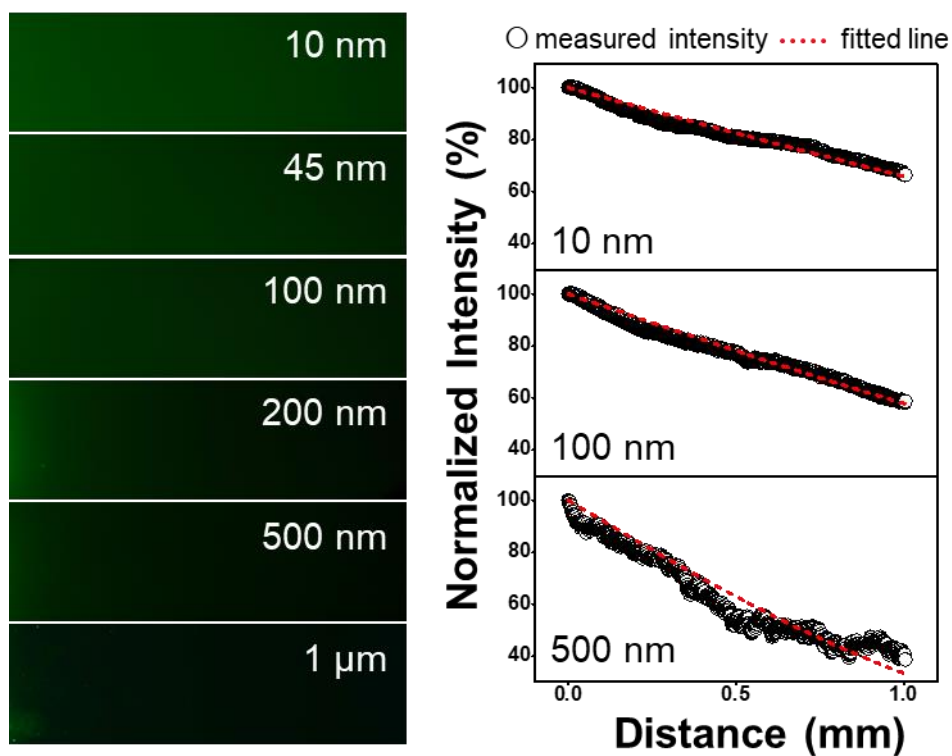


Figure 3.9. In the 0.2% collagen gel, a concentration gradient appeared. The green fluorescence intensities of MSNs of various sizes were normalized and fitted with Fick's second law solutions. MSNs of sizes of 10, 100, and 500 nm were displayed.

3.3.4 Calculation of diffusion coefficient (D)

The rate of concentration accumulation inside an area is proportional to the local curvature of the fluorescence concentration gradient, according to Fick's second law of diffusion. During perfusion, the concentration situation at the interface where MSNs are injected inside the chip is constant, while diffusion inside the gel is non-steady, allowing us to apply Fick's second law. Furthermore, it is assumed that the concentration of pharmaceuticals or nanocarriers in the blood vessels remains constant throughout time, and so the diffusion phenomena on the chip can mimic the actual diffusion process from the real vessels. Because the speed of particles traveling through collagen varies, so does the degree of the concentration gradient. Using Fick's second law, the fluorescence pictures were converted to grayscale and normalized for plotting and fitting. Left graphs in figure 3.9 depicts the normalized intensity from left images as well as fitted line examples of 10, 100, and 500 nm particles. Figure 3.10 shows the calculated diffusion coefficients (D) after exposing each data point to the same method. The D value decreases as the size of the MSNs increases. The mean value of the smallest particle (MSN with a particle size of 10 nm) was $2.98 \times 10^{-10} \text{ m}^2/\text{s}$, while the mean value of the largest particle (MSN with a particle size of 1 μm) was $1.14 \times 10^{-11} \text{ m}^2/\text{s}$. This means that as the size of the MSN rises, the diffusion rate per second drops.

This means that as the size of the MSN rises, the diffusion rate per second drops. Even though there were some variations in 500 nm particles in

Figure 3.9., we provided that the fitted result from Fick's second law was evident for MSNs. According to Jia et al., particles as small as 1 μm may exhibit Brownian motion[64]. However, diffusional displacement and particle sedimentation compete by size, with sedimentation becoming dominating with particles 500 nm or bigger[65]. Given the thickness of the collagen injected in the chip ($\sim 200\ \mu\text{m}$), particle sizes larger than 500 nm would diverge from solely diffusional motion when seen horizontally. It is difficult to anticipate whether MSNs follow perfect Brownian motion or display a departure due to physiochemical variety and the experimental environment, such as their porosity, weights, functional groups, or temperature[66-68], using only a single parameter, particle size. Furthermore, particle dynamics can be altered by solution ionic strengths or electrostatic interactions between particles under physiological settings[69, 70]. As a result, MSNs with 500 nm or bigger in our research do not precisely follow the diffusional motion defined by equation (1). Analyzing the transportation behavior of MSNs in the LOC platform entails more than just measuring the diffusion coefficient; it also entails determining the size range where diffusion or sedimentation is dominant, which can provide data and information critical to the selection and/or screening of drug carriers for *in vivo* studies.

The experimental conditions were set to inhibit interstitial flow in order to purely measure diffusional properties in this study, but subsequent research studies involving the effects of interstitial flow or circulation of body fluids are required, especially for larger particles, to improve the LOC

platform and make it more *in vivo*-like.

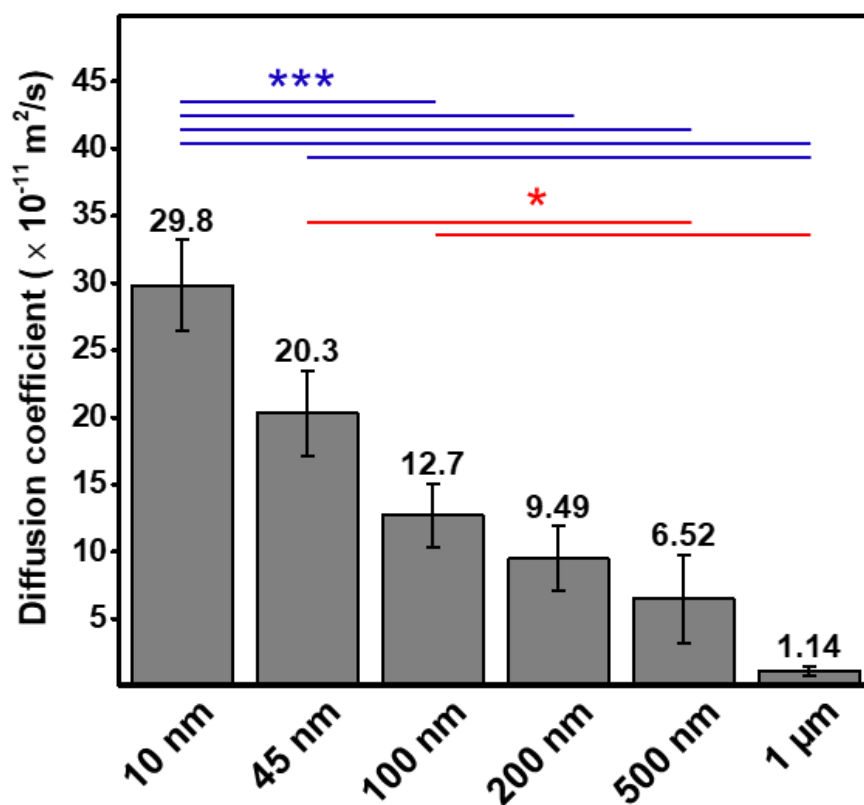


Figure 3.10. Diffusion coefficients (D) of the MSNs are plotted in bar graphs.

(* $p < 0.05$ and *** $p < 0.001$)

3.3.5 Diffusion profiles of MSNs and their applications

D values alone do not provide intuitive information about the speed of diffusion. Therefore, based on the results shown in Figure 4d, the concentration profiles of MSNs of each size at $t = 3$ h were plotted (figure 3.11.). Profile graphs provide information on the spatial distribution of the particles compared to the boundary value ($C_s=100\%$) at a certain time. It is evident that, differences in the profile of each size of MSN exist, and it is noteworthy that the concentration of MSNs with a size of > 200 nm is below 50% when the distance from a vessel is $100\ \mu\text{m}$ even after 3 h. For example, because the diffusion distance to the tumor is usually up to $100\ \mu\text{m}$ [71], if the size of MSNs loaded with antitumor drugs exceeds 200 nm, the concentration of MSNs at the margin of tumors is still less than half of the concentration in the blood vessels even after 3 h. This can be the clue of the huge discrepancy between *in vitro* cell tests and *in vivo* tests: if cells are cultured in a homogeneous liquid medium with even spatial distribution of MSNs loading anti-cancer drugs, denoted as $C_{in\ vitro}$, all cells are affected by the same drug concentration value, $C_{in\ vitro}$; however, in *in vivo* tests, even if a dose of the same drug is designed to be $C_{in\ vitro}$ at the blood vessel for a certain time period, the actual concentration of the drug at the margin of a tumor $100\ \mu\text{m}$ away from the vessel would be less than $0.5 \times C_{in\ vitro}$ after 3 h. Moreover, as solid tumors are denser than normal tissues, material transport by convective flow is negligible, and diffusion is much slower inside the tumor[72]. Therefore, new advanced cell-based methods which can give numerical information

about the diffusion behavior of drug or drug carriers and bridge in vitro and in vivo tests are strongly required. Indeed, the microfluidics chip platform provides experimental conditions close to those in *in vivo* tests and sets up virtually ideal boundary conditions sufficient for diffusion experiments (figure 3.12.). Most importantly, as the analyses methodologies consisting of fluorescence profile capturing, image processing, and least-squares fit to the well-known solution are quite simple and can predict the quantitative spatiotemporal distribution of drug or drug carriers, our results can easily be applied to various pathological tissue model studies testing a large number of drug or drug carrier candidates.

D values alone do not give obvious information regarding diffusion speed. As a consequence, the concentration profiles of MSNs of each size at $t = 3$ h were plotted based on the data given in Figure 4d (figure 3.11.). Profile graphs show the geographic distribution of particles in relation to the boundary value ($C_s = 100\%$) at a given time. It is clear that there are variances in the profile of each size of MSN, and it is worth noting that the concentration of MSNs with a size of > 200 nm is less than 50% when the distance from a vessel is $100\text{ }\mu\text{m}$, even after 3 h. Because the diffusion distance to the tumor is often up to $100\text{ }\mu\text{m}$, if the size of MSNs loaded with anticancer medications exceeds 200 nm, the concentration of MSNs at the tumor margin is still less than half of the concentration in blood vessels even after 3 h. This could be the explanation for the large disparity between in vitro and in vivo cell tests: if cells are cultured in a homogeneous liquid medium even with spatial

distribution of drug-loaded MSNs, denoted as $C_{in\ vitro}$, all cells are affected by the identical drug concentration level, $C_{in\ vitro}$; In vivo experiments, however, even if a dosage of the same medication is set to be $C_{in\ vitro}$ at the blood vessel for a given time period, the actual concentration of the drug at the margin of a tumor 100 m distant from the vessel after 3 h would be less than $0.5 \times C_{in\ vitro}$. Furthermore, because solid tumors are thicker than normal tissues, convective flow transport is minimal, and diffusion is significantly slower inside the tumor. As a result, more sophisticated cell-based approaches that can provide numerical information regarding drug or drug carrier diffusion behavior and bridge *in vitro* and *in vivo* studies are urgently needed. Indeed, the microfluidics chip technology simulates *in vivo* testing circumstances and establishes almost optimal boundary conditions for diffusion investigations (figure 3.12.). Most importantly, because the analysis methodologies of fluorescence profile capture, image processing, and least-squares fit to the well-known solution are quite simple and can predict the quantitative temporal and spatial distribution of drug or drug carrier candidates, our findings can be easily applied to various pathological tissue model studies testing a large number of drug or drug carrier candidates.

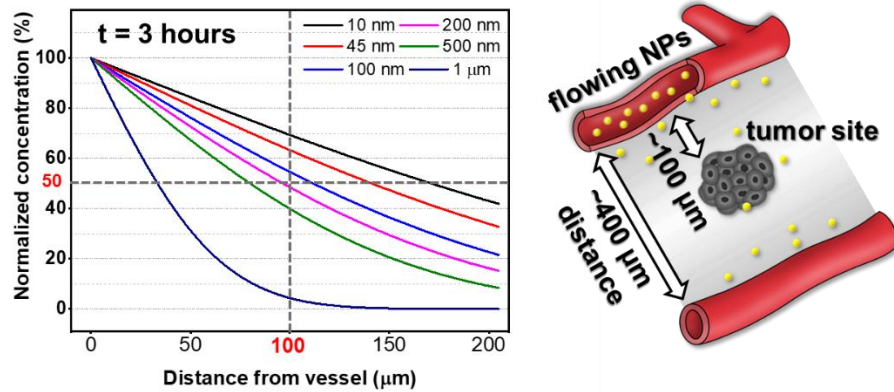


Figure 3.11. When $t = 3$ hours, 50% or more of the original concentration is dispersed in diverse ways at 100 μm, the distance from the general blood artery to the cancer tissue.

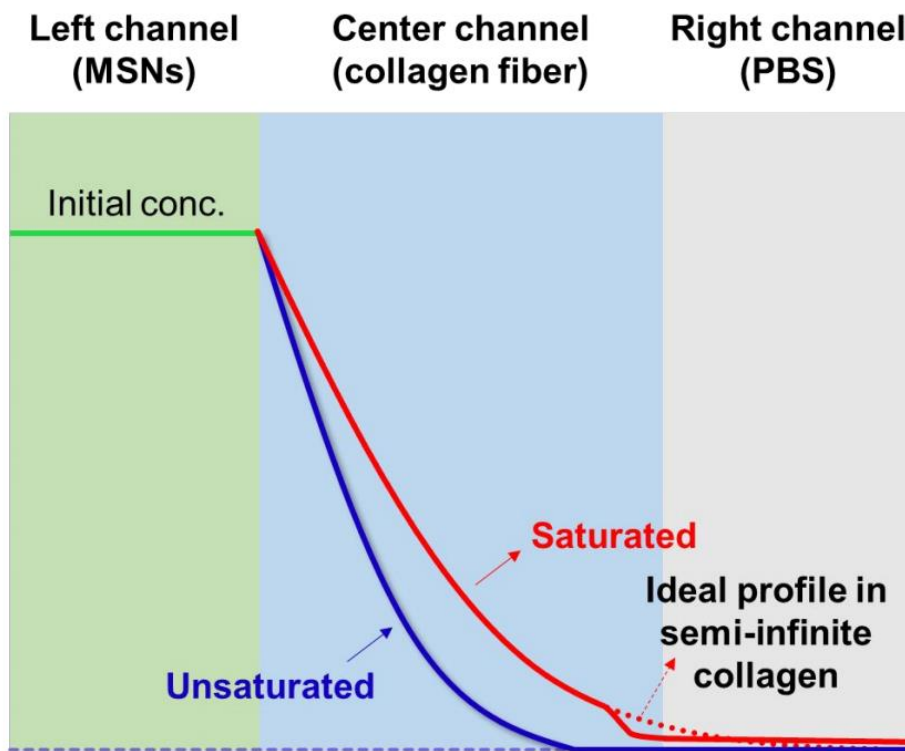


Figure 3.12. The theoretical concentration profiles that can be found within the chip. In order to obtain the most accurate answer from equation (1), it is important that the MSNs do not become completely saturated inside the collagen gel ("Unsaturated," blue line). This allows the collagen gel to be thought of as a semi-infinite medium. When MSNs enter the right channel, which is filled with PBS and has a much faster diffusion rate, the concentration profile, which is denoted by the red line and labeled "Saturated," does not match the profile that would be ideal, which would be denoted by the red dotted line if the medium were semi-infinite.

3.4. Conclusion

We investigated how MSNs diffused in collagen that mimicked the behavior of tissue and predicted their spatiotemporal behavior by utilizing the diffusion coefficient that was obtained in the LOC platform. Inducing the diffusion of fluorescent MSNs in the LOC allowed for the production of gradients in tissue-mimicking collagen. These gradients were established by modulating the concentrations of MSNs in each channel. By fitting the fluorescence profiles to the solution of Fick's second law while using the collected fluorescence images, it was possible to determine the D of the MSNs as a function of their size. MSNs had a diffusion coefficient that ranged from $2.98 \times 10^{-10} \text{ m}^2/\text{s}$ (when their size was equal to 10 nm) to $1.14 \times 10^{-11} \text{ m}^2/\text{s}$ (when MSNs size was equal to 1 μm). The spatiotemporal profiles of MSNs were calculated using the obtained D , and it was demonstrated that the concentration of MSNs with a size $> 200 \text{ nm}$ at $100 \mu\text{m}$ from the gel–liquid interface will remain $< 50\%$ of that in the vessel-mimicking channel even after three hours has passed. This was demonstrated by the fact that the concentration of MSNs with a size $> 200 \text{ nm}$ at $100 \mu\text{m}$ from the gel–liquid interface was calculated. In addition, the procedures for analysis and prediction that are based on the processing of fluorescence profile images and a least-squares fit to the well-known solution are relatively straightforward, and it is highly anticipated that our findings will be able to be used to resolve the discrepancy between the concentration of drugs in the vessel and at the

lesion. Calculating the diffusion coefficient of potential medication candidates prior to doing trials on animals would help bridge the gap that currently exists between *in vitro* testing and experiments on animals. This study has the potential to be economically beneficial in terms of both time and cost, as well as to enable the successful design of *in vivo* testing, and it may replace some aspects of animal trials.

Chapter 4. Transportation of Nanocarriers

4.1. Introduction

MSN transport starts from the inside of blood vessels[8, 24, 73]. Efficiency evaluation of drug-loaded MSN is highly dependent on animal experiments, and animals injected with drugs are evaluated on a tissue-by-tissue basis using imaging techniques such as whole-body imaging[74].

Although it is credible to say the degree to which the number of nanoparticles has been delivered to a certain tissue through tissue evaluation, in fact, the evaluation of these tissue units has limitations. It is difficult to determine whether the drug is delivered to the inside of the tissue or to the blood vessel. When looking at the circulation system of our body, the particles flowing through the blood vessels exit the blood vessels and reach the cells, but it is difficult in animal experiments to confirm whether they have exited the blood vessels[74-77]. Therefore, in this chapter, I divided the steps into detailed modeling.

Whether or not nanoparticles penetrate the endothelial barrier in blood vessels was modeled after calculating the diffusion coefficient as in the previous chapter. This time I used two types of chips. These two chips imitate the blood vessel part in the figure 4.1. and the ECM part where nanoparticles diffuse, respectively. First, blood vessels were formed inside the chip to check whether nanoparticles passed through the blood vessels. With the second chip, the diffusion coefficient of nanoparticles in the ECM gel was determined.

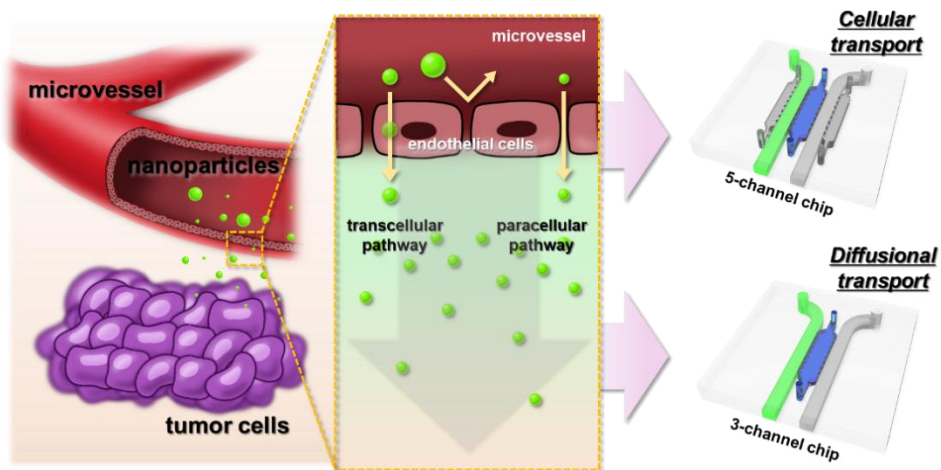


Figure 4.1. Schematic images of tumor microenvironment (TME) and microfluidics chips which could represent microvessel area and mimic diffusional transport.

4.2. Experimental Procedures

4.2.1. Materials

The following chemicals were acquired from Sigma-Aldrich in the United States: cetyltrimethylammonium bromide (CTAB), tetramethylorthosilicate (TMOS), tetraethyl orthosilicate (TEOS), triethanolamine (TEA), N-hydroxysuccinimide (NHS), and 1-ethyl-3-(3-dimethylaminopropyl)-carbodiimide (EDC). The 5-(and 6-)carboxyfluorescein, often known as FAM, was acquired from Thermo Fisher Scientific in the United States of America. Dow Corning in the United States supplied us with the SYLGARD® 184 that was needed for the chip production. In order to prepare the polydopamine coating, dopamine hydrochloride was acquired from Sigma-Aldrich in the United States. Corning, located in the United States, supplied the acid-treated rat tail collagen type I. Thermo Fisher Scientific was the vendor for the acquisition of Alexa Fluor® 555 NHS ester for the purpose of collagen labeling.

4.2.2. MSNs fabrication

MSNs were created using a modified version of a sol-gel process that had already been published[10, 56]. As a check for the right catalytic reaction's pH conditions, CTAB with TMOS or TEOS was employed. A reaction between CTAB (83.8 mg) and TMOS (0.096 mL) for 10 nm particles took place at room temperature in an ammonium hydroxide/ethanol solution.

MSNs with a 45 nm particle size were created at 40 °C in a solution containing TEA (0.028 g), CTAB (0.33 g), and TEOS (0.73 mL). For MSNs of 100 nm in size, CTAB (4.16 g) and TEOS (0.36 mL) were combined and heated to 30 °C in an ammonium hydroxide/methanol solution. At room temperature, TMOS (1.3 mL) was added to CTAB (4 g) together with dissolved sodium hydroxide/methanol solution to create MSNs in the sizes 200-nm, 500-nm, and 1- μ m. The methanol/water molar ratios in this process were 1:2.26, 1:1.7, and 1:1. The gathered items were calcined at 550 °C for 4 hours in a furnace to eliminate the template CTAB. Finally, using the NHS/EDC reaction between the MSNs and NHS-fluorescein, FAM-tagged MSNs were created[55].

4.2.3. Chip fabrication and channel coatings

Polydimethylsiloxane (PDMS) was used in the soft lithography process to create three and five channel PDMS chips on silicon wafers with the SU-8 design. After degassing the mixture, Sylgard[®] 184 and its curing agent were combined in a 10:1 (w/w) ratio and put into the silicon wafer mold. Over two hours, the PDMS was cooked in a 70 °C oven. After being removed from the mold and allowed to firm, the PDMS was cut to the correct size before being punched to allow for the injection of gels or liquids. Following oxygen plasma treatment, the PDMS fragments developed covalent bonds with the cover glasses. Following each other, distilled water and 70% ethanol was used to wash the whole batch of PDMS chips.

To prevent MSNs from adhering to the bottom and wall of the channel of the chips, tetraethyl orthosilicate (TEOS) coating was applied (10:1 v/v, in ethanol) to the left channels of the 3-channel chips for an hour. Two five-minute ethanol washes were performed on the TEOS residue. In order to strengthen the link between the PDMS wall and the collagen/fibrin fibers and prevent the shrinkage effect during the gelation of the collagen, polydopamine (PDA) coating was performed for two hours in the center channels of both 3-channel-chips and 5-channel-chips. To create a 2.0 mg/mL working solution, distilled water was mixed with 10mM Tris-HCl to dissolve a dopamine hydrochloride. The darkened working solution was coated for two hours before being cleaned three times with distilled water and allowed to air dry.

4.2.4. Cell preparation

Red fluorescence protein expressing human umbilical vein endothelial cells (RFP HUVECs) were cultured in EGMTM-2 Media (Lonza, Switzerland) and human normal lung fibroblast (hNLF) were cultured in FGMTM-2 (Lonza, Switzerland). Each vial of the cells was thawed and kept in the humidified cell culture incubator (37 °C, 5% CO₂) at least for 48 hours to stabilize the cells. RFP HUVECs and hNLF passage between 3 to 7 were used in this study.

4.2.5. Gel preparation and cell embedding

Two types of gels – fibrin and collagen mixture gel for diffusion and cell embedded mixture gel for vessel formation – were mixed to be used. For diffusion matrix, the fibrin gel and collagen gel were prepared at the concentration of 0.2% each, and the same volume was mixed to 1:1. The final concentration of each gel became 0.1%. For cell embedding (vessel formation), the concentration of the fibrin and collagen mixture is the same with the diffusion matrix, but RFP HUVECs or hNLF were added to the solution before gelation. The final cell density of RFP HUVECs was $3.0 \sim 3.5 \times 10^6$ cells/ml in the collagen and fibrin mixture and that of LF was $5.0 \sim 6.0 \times 10^6$ cells/ml. For both chips, containing cells or not, are incubated in the 37 °C humidified cell culture incubator to promote sol-gel process. After the gelation, for the cell containing gels, the cells are placed three dimensionally from the bottom to the top of the channel (figure 4.2.).

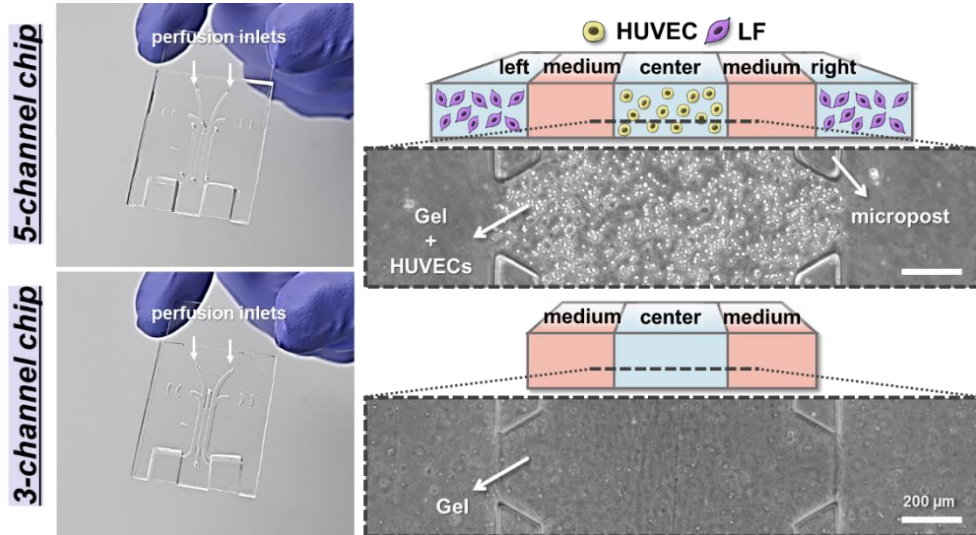


Figure 4.2. The 5-channel chip for HUVEC culture and 3-channel chip for diffusion study. Both chips were used in this study to model the MSNs penetration and diffusivity.

4.2.6. Perfusion preparation

The gel or cell containing chips were placed in the 37 °C humidified cell culture incubator and the syringes with tubes were connected to the chips. As shown in figure 4.3., the liquid containing syringes were injected with syringe pump (Harvard Apparatus, USA) at the flow rate of 450 μ l/h. As shown in figure 4.3., MSNs flew through the left channel and pure PBS flew through the right so that the diffusion of MSNs occurs from left to right of the gel matrix.

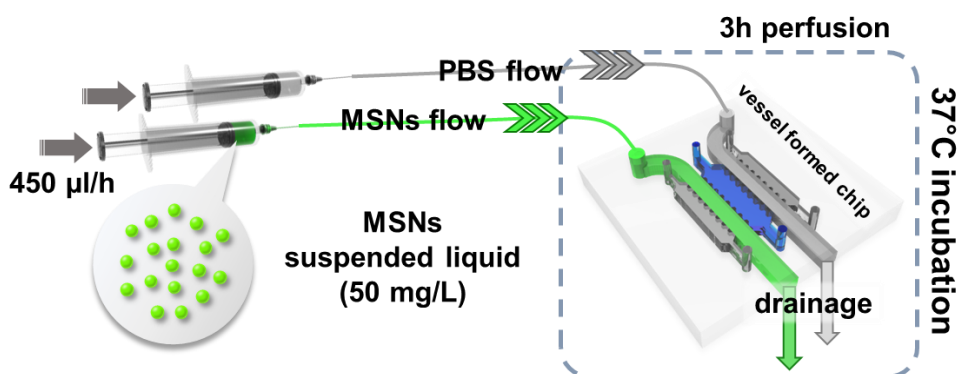


Figure 4.3. The perfusion method to 5 channel chip. The microvessels were formed in the center channel of the chip (blue channel). When MSNs are applied to the left channel and PBS perfusion is applied to the right channel to the chip on which microvessels have been created for 72 hours, nanoparticles flow into the created vessels.

4.2.7. Gel dyeing and mesh imaging

0.1% Alexa FluorTM 555 carboxylic acid, succinimidyl ester (Thermofisher, USA) of total volume were added to the solution of fibrinogen or collagen, then the gelation was done. The dyed fibers were imaged with confocal laser scanning microscope (Zeiss, LSM 700, Germany) three dimensionally.

4.2.8. Cell and MSNs imaging

Imaging of cell and MSNs in the vessel chip was done with the confocal microscopy as used in mesh imaging. The image of MSNs diffusion was obtained from fluorescence microscopy (Olympus, IX71)

4.2.9. Connection of the chip to the syringe pump

The MSNs containing PBS were sonicated for a minute to alleviate the aggregation among particles. The MSNs containing syringes were interconnected with the chips by using Tygon[®] tubes (USA, ID 0.020/OD 0.060 in.).

To avoid the saturation of the MSNs concentration in the gel, small particle groups (10, 45, and 100 nm) were perfused for three hours and the other particle groups (200 nm, 500 nm, and 1 μ m) were perfused for six hours. The saturated results would result the unreliable result after fitting to the solution of Fick's second law.

4.2.10. Image analysis

All the measured data were averaged and standard error (\pm SEM) was calculated as well. The sizes of nanoparticles were measured using ImageJ software (NIH, USA). By measuring the length of the straight lines that intersect the particles, ImageJ was used to collect at least four particle sizes in each image. After averaging the data, it was shown. Using ImageJ software, the fluorescence profile in the middle collagen-filled channel (width: 1,000 μ m) was gathered and examined for diffusion modeling. Red, Green, and Blue channels were separated from each of the center channel images, which had been cropped to $1.0 \times 0.3 \text{ mm}^2$ in size. The intensity levels at point x in the rectangular images were then averaged after just the green channels had been examined. Pixels were translated to actual distance and the grayscale image profile of the green channel was applied. Intentionally placed in the upper-left corner of the image was the original intensity. After the beginning intensities were normalized to 100%, the gradients were fitted using MATLAB (MathWorks, USA) using the diffusion model described below to obtain the diffusion coefficient. Unnecessary background signals were removed when imaged.

4.2.11. Diffusion model

We applied Fick's second law to determine the diffusion coefficient (D) of the MSNs in the collagen matrix. The surface concentration of the nanoparticles at the lesion (C_s at $x = 0$) and the bulk concentration in the blood

(C_0 at $x = \infty$) were thought to remain constant when a drug was injected into the body.

$$\frac{\partial C}{\partial t} = D \frac{\partial^2 C}{\partial x^2}$$

For $t = 0$, $C = C_0$ at $0 \leq x \leq \infty$

For $t > 0$, $C = C_s$ (the constant surface concentration) at $x = 0$

$$C = C_0 \text{ at } x = \infty$$

Setting the limit by applying boundary conditions of concentration in our study condition yields the solution to Fick's second law:

$$\frac{C_x - C_0}{C_s - C_0} = \text{erfc}\left(\frac{x}{2\sqrt{Dt}}\right) = 1 - \text{erf}\left(\frac{x}{2\sqrt{Dt}}\right) \quad eq(1)$$

where C_x is the nanoparticle concentration at distance x from the sol-gel interface after time t . Here, the surface and bulk concentrations were $C_s = 100 \mu\text{M}$ and $C_0 = 0 \mu\text{M}$, respectively, and we measured the concentration of the fluorescence of MSNs at $x = 0$ to 0.001 m for $t = 10,800 \text{ s}$. A least-squares fit of the complementary error function to the concentration data gives diffusion coefficients for different particle sizes ranging from 45 nm to $1 \mu\text{m}$; the curve-fitting algorithm finds an optimal estimate by finding the minimum of the unconstrained multivariable function, $C(t) - (1 - \text{erf}(\frac{x}{2\sqrt{Dt}}))$, using a derivative-free method

4.2.12. Drug efficiency

The equation below was used to calculate the relative drug

effectiveness. The data came from the outcomes of the animal tests.

$$\text{Relative drug efficiency} = \frac{\%P_{control} - \%P_{group}}{\%P_{control} - 100} \times 100\% \quad Eq(4)$$

Where $\%P_{control}$ indicates percent point of control and $\%P_{group}$ indicates percent point of each experimental group

4.3. Results and Discussion

4.3.1. Fibrin and collagen mixture matrix

Because of the lack of retraction and the abundance of integrin receptors, many studies use fibrin as a matrix for microvessel formation, angiogenesis and vasculogenesis[78, 79]. However, since the lesion we mimicked in this study was cancerous tissue, collagen, the most abundant ECM in cancer tissue[49, 80], was mixed with fibrin 1:1 and HUVECs were cultured. For both vessel formation and diffusion study, 0.2% mixture matrix (0.1% for fibrin, 0.1% for collagen) was adopted. The mesh size was determined by fluorescence imaging (figure 4.4.(a)). The mesh size analysis from ImageJ, it has $\sim 5\ \mu\text{m}$, so MSNs could be transported through the ECM matrix. If the collagen mesh is the same size as or smaller than the MSNs, it can act as a barrier to MSNs transport through the matrix[43, 51]. To confirm that there is no retraction or shrinkage of the matrix, the 3D stacked image was obtained from confocal microscope. Figure 4.4.(b) shows the homogeneity of the matrix. The mixture gels inserted into the center channel with or without cells were homogeneously distributed due to PDA coating inside the channel. SEM image also shows the matrix fiber was formed adequately (figure 4.4.(c)).

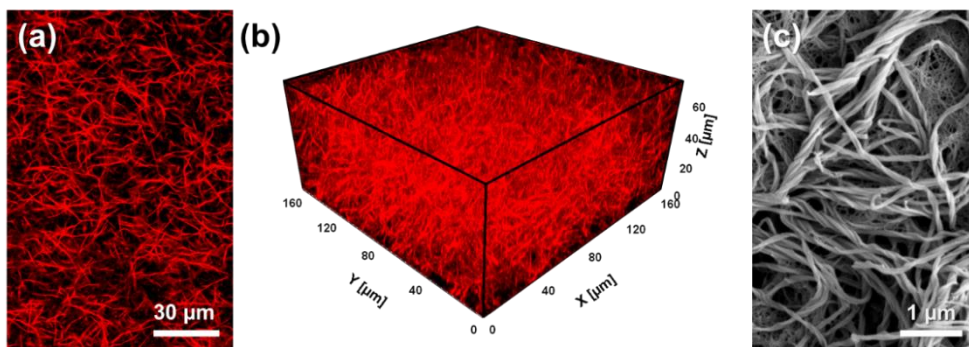


Figure 4.4. The mixture matrix of collagen (0.1%) and fibrin (0.1%). (a) The dyed mixture was captured with confocal microscopy. (b) The homogeneity of the gel component is proven from the z-stacked images. (c) Higher magnification SEM image was captured to show the collagen and fibrin fiber formed together.

4.3.2. Vessel formation in three types of gels

Instead of fixing and dyeing the normal HUVECs to image the vessels formed in the chip, RFP HUVECs were used in this study instead of normal HUVECs to image the live cells. After incubating 72 h, the microvessels were formed inside the center channel. The RFP HUVECs were connected (figure 4.5.(a)) by interactions of themselves[81] and helped forming by cytokines[31, 38] from LFs in the left and right channel of 5-channel chip. Without fixing the cells, we could observe the microvessels with confocal microscopy (figure 4.5.(b))

The vessel formation was also compared in three types of gels, which are fibrin only, collagen only and the mixture matrix. Comparing with the fibrin gel, which is the most adequate ECM to form the microvessels, the mixture matrix also shows the good vascular shape (figure 4.6.).

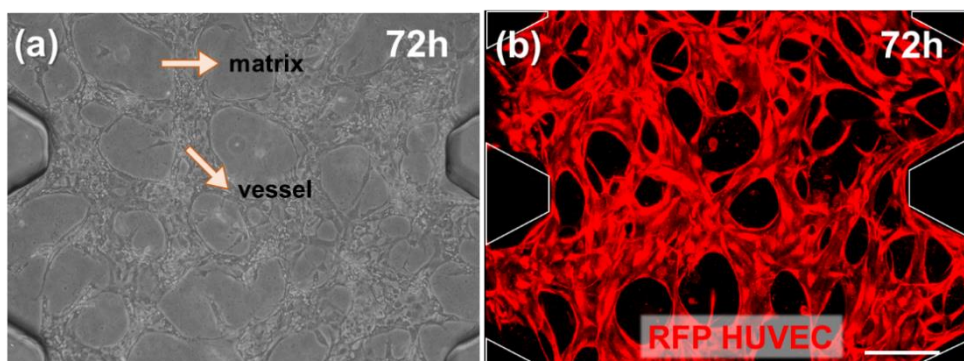


Figure 4.5. Well-formed microvessel in center channel of 5-channel chip. As a result of generating microvessels for 72 hours in the fibrin and collagen mixture matrix, it was confirmed that vessel formation was good and HUVEC connection was well established.

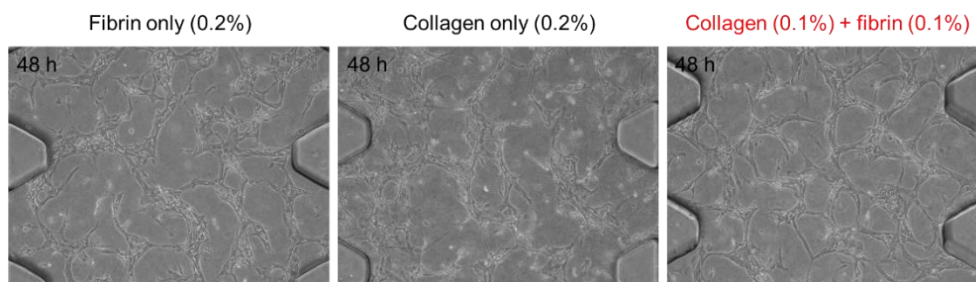
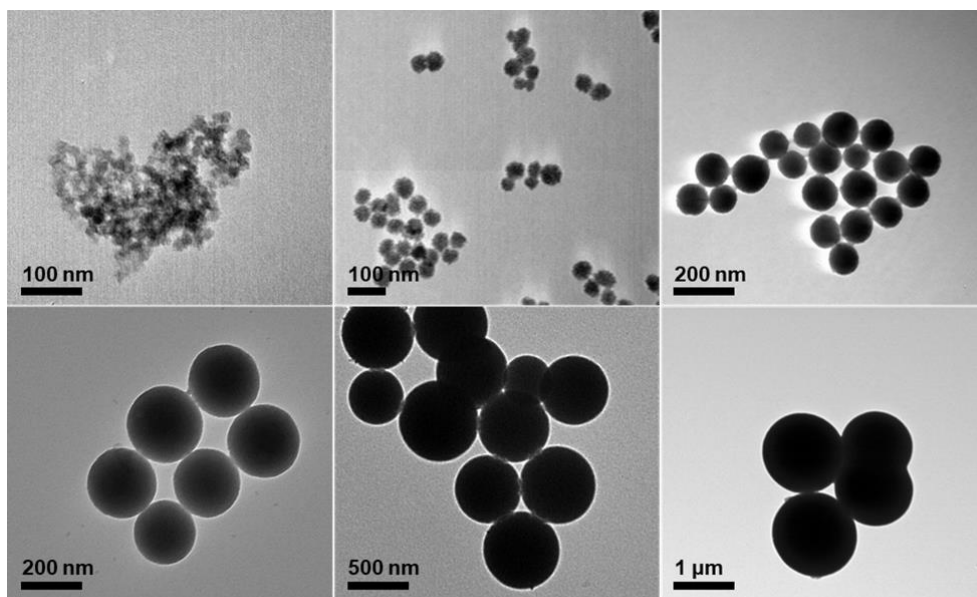


Figure 4.6. Comparison of microvessel formation in three types of ECM gels.

To form the microvessels with HUVECs, fibrin matrix was adopted to make the well-formed microvessels in vitro. However, we targeted tumor microenvironment, collagen was also mixed with fibrin. The mixture matrix shows the similar tendency of vessel growing, comparing with fibrin only matrix.

4.3.3. MSNs characterization

In figure 4.7., TEM images of MSNs with six sizes of particles – 10, 45, 100, 200, and 500 nm and 1 μm – are shown in figure 4.7. The manufactured MSNs had pores with a size of around 3 nm, a volume of 3 cc/g, and a large surface area of 1,908 m^2/g , which made it easier for medications to be loaded into the pores, according to nitrogen sorption analysis. All of the particles had a negative surface potential that was caused by the SiOH surface group[55].



Diameter (nm)	Mean pore size (nm)	BET surface area (m ² /g)	Pore volume (cc/g)	Zeta potential (mV)
10	2.98	1908	3.01	22.4±1.1
45	2.94	1652	2.97	23.1±0.8
100	3.02	1476	3.02	23.5±0.3
200	2.97	1361	3.11	21.8±1.6
500	3.05	1110	3.04	21.9±0.7
1000	2.88	986	3.14	22.7±1.2

Figure 4.7. TEM mages of all sizes of MSNs (10 nm, 45 nm, 100 nm, 200 nm, 500 nm, 1 μm) were obtained. Also, other features of MSNs such as mean pore size, BET surface area, pore volume and zeta potential were characterized.

4.3.4. MSNs penetration through vessel walls

As shown in figure 4.8., MSNs are injected into the blood vessel grown chip through the left channel, and at the same time, PBS without MSNs is injected into the right channel. After 3 hours perfusion, the microvessel was observed as a low-magnification image. From the smaller sizes particles – 10nm and 100 nm, it was confirmed that the smaller MSNs passed through the blood vessel wall. However, there were few particles that have passed through the blood vessels for the 1 μ m size particles and as a result of quantifying the image data, it was shown that they have different penetration rates as in figure 4.8.(e). 10 nm particle has 31.48 %, and 100 nm particle has 20.77 % and 1 μ m has 8.20 %, respectively. Also, each particle has statistically significant values each other. Additionally, we have checked the penetration tendency of all size of MSNs in the higher magnified images. 10, 45, 100, 200 nm MSNs positioned from inside of the vessel (yellow arrow) to outside of the vessel (cyan arrow) in figure 4.9. Otherwise, most of 500 nm and 1 μ m sized MSNs positioned inside the vessel.

From the observations of the chip from above, the X-Y plane, we could see MSNs with a size of 500 nm or larger have MSNs staying inside the blood vessels. Similarly, when looking at the cross-section view, the larger particles mainly located inside the lumen formed as tubes, so it is difficult to see it coming out of the blood vessel. From this result, it can be concluded that there is a large limit in the size between 200 nm and 500 nm.

Depending on the tightness of the endothelial barrier, the particle

penetration rate could vary. If targeting tight tissues such as the blood brain barrier, penetration tendency of particles or drugs could be observed after culturing the vessels with adequate condition of BBB[22, 33, 82]. Also, if simulating actual cancer tissue, it can be observed that the tendency of particles to pass through at the more loosened junction because of the inflammation effect[15, 83].

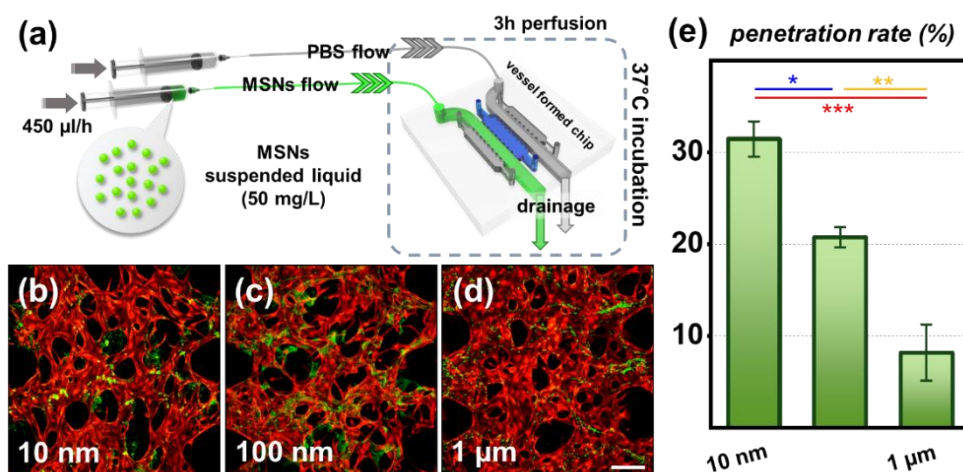


Figure 4.8. The endothelial barrier penetration of each size of MSNs. (b) 10 nm and (c) 100 nm MSNs tend to show leakage from the microvessels, but (d) 1 µm MSNs flow through the microvessel rather than pass through the barrier. (e) The penetration rate was calculated based on (a), (b) and (c). Each group are statistically significant (* $p < 0.05$, ** $p < 0.01$ and *** $p < 0.001$).

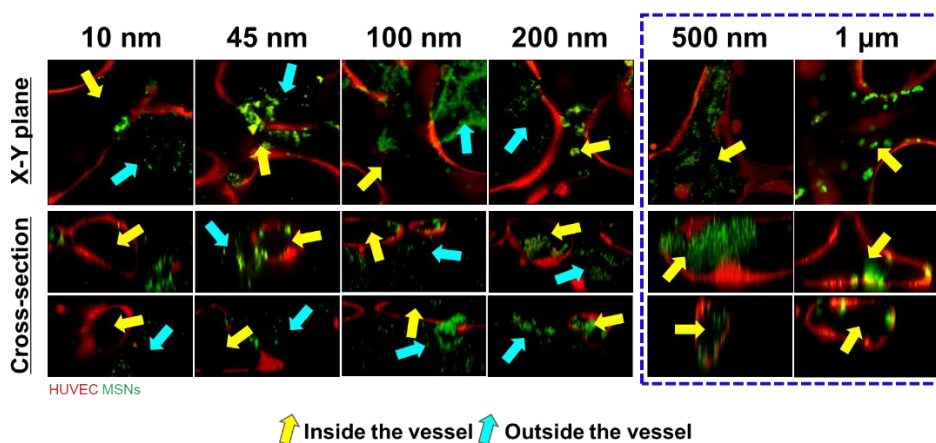


Figure 4.9. Confocal microscopy images of each size of MSNs were captured to show X-Y plane and cross-section (X-Z or Y-Z planes) so that the leakage from the lumen can be demonstrated. From 10 nm to 200 nm, the number of MSNs located outside of the microvessels. However, for 500 nm and 1 μm sizes, more MSNs remained inside the vessel, which indicates that the larger size of the particles are hardly able to pass through the vessel barriers. The yellow arrows indicate the inside the vessel and the cyan arrow indicates the outside of the vessel

4.3.5. Diffusion coefficient calculation

The process after particles exit from the blood vessel is for the MSNs to diffuse from the vessel wall to the tissue[84]. To figure this out, flow was applied to the left and the right channel of the 3-channel chip and the samples were incubated for a certain time to obtain the results (figure 4.10.(a)). Here, we divided the MSN groups into 2, which are 3 hours perfusion group (for 10 nm, 45 nm, 100 nm group) and 6 hours perfusion group (200 nm, 500 nm, 1 μ m). To perform the fitting in the solution of Fick's second law, the boundary condition should be maintained and the concentration should remain unsaturated in the matrix[55]. After inducing the diffusion for 3 hours and 6 hours for each group, we could observe the concentration gradient as shown in figure 5B. From the fluorescence gradient images, the tendency of fluorescence gradient formed is different for each size. After quantifying each particle to gray scale based on the image and plotting it with normalize concentration, the plot was fitted to the solution of Fick's second law (figure 4.10.(b)). Figure 4.10.(c) shows the representative plotted graphs of 10 nm, 100 nm and 1 μ m among all sizes of MSNs. As indicated in figure 4.11.(a), the larger the size of MSNs the lower the value of diffusion coefficient. These values mean that the smaller particles transport faster to the targeted lesion,

Through this chip study, we were able to quantitatively find out the D values of 6 sizes of MSNs. Therefore, as shown in figure 4.11.(b), it is possible to predict what concentration value each MSNs will have through the profile at a specific distance and a specific time.

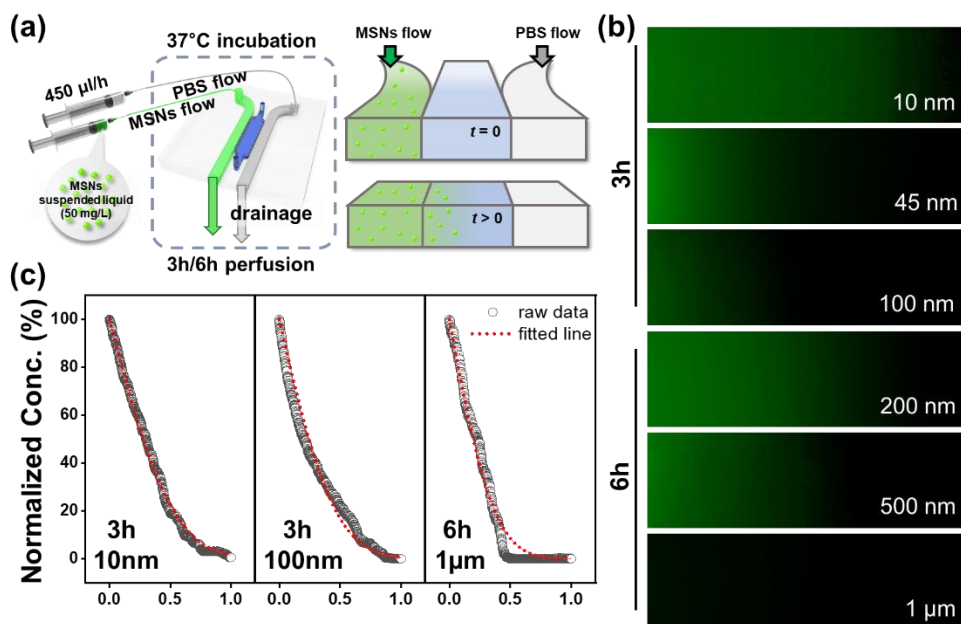


Figure 4.10. (a) MSNs perfusion at a flow rate of 450 $\mu\text{l/h}$. (b) The particles of the small size (10, 45 and 100 nm) were perfused for 3 hours, and the particles of the relatively large size (200 nm, 500 nm and 1 μm) were perfused for 6 hours and then imaged. (c) Based on this, gradient is graphed and the result of fitting to the solution of Fick's second law.

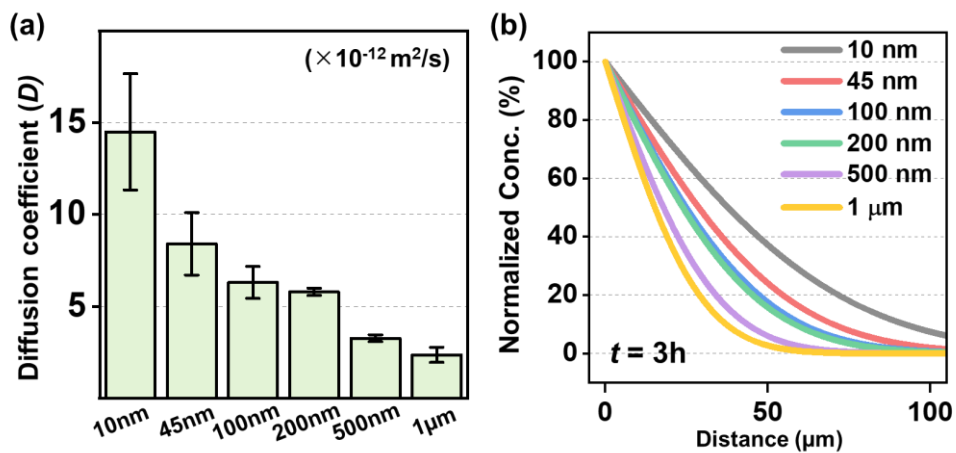


Figure 4.11. D of MSNs in ECM including fibrin has a value with an order of 10^{-12} because the mesh size was small. Small sized particles have a relatively high D value. Based on this, the profile at $t = 3$ was plotted by normalizing the initial concentration.

4.3.6. Animal testing results

As a result of animal experiments (figure 4.12.), simple drugs and drug-loaded nanoparticles were injected into mice transplanted with cancer tissue, and the size was observed for 10 days. Here, control is a group of mice that do not receive any drug treatment. PTX was the anti-cancer drug paclitaxel, and the rest of the nanoparticles were loaded with the same amount of paclitaxel even though they had different sizes. Compared to injecting only simple drugs, it can be seen that the nanoparticles and the smaller the size are more effective.

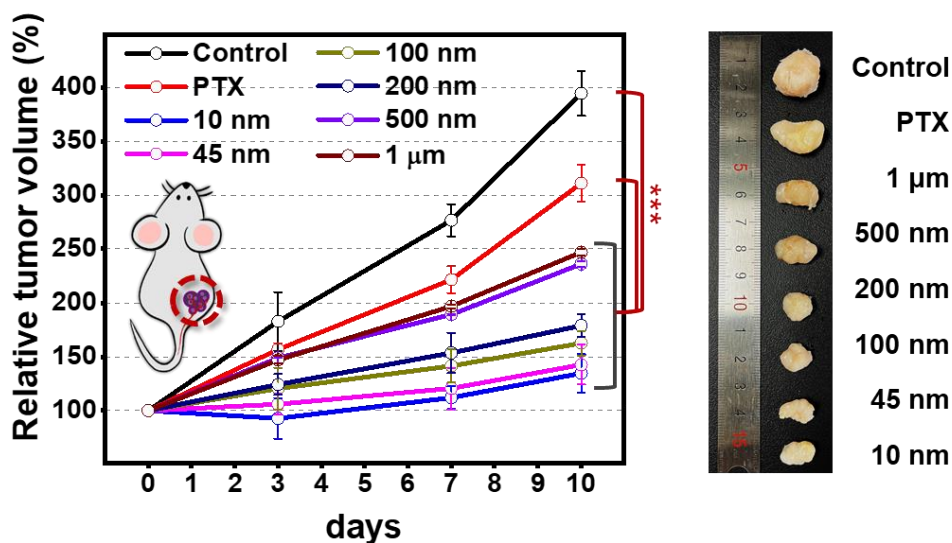


Figure 4.12. Animal testing result with using various sizes of MSNs and not using MSNs. Control group indicates the no drug injection. PTX (paclitaxel) indicates the drug only group. All sizes of the MSNs have the same volume of PTX inside the pore of them (***) $p < 0.001$). MSNs are more effective than simple drugs, and the smaller the size MSNs, the better effect in tumor.

4.3.7. Comparison of drug efficiency and concentration profile

Based on figure 3B, the relative drug efficiency was calculated based on $eq(4)$ and the values were plotted in figure 4.13. In each experimental group compared with the control group, the PTX showed lower efficiency compared to the case of using MSNs, and it confirmed that the efficiency is better at a small size of MSNs. Additionally, it once again shows that loading drugs into MSNs is more effective than simply injecting PTX. The results of animal experiments in which small MSNs are more effective than the larger ones are shown to correspond to the results of drug efficiency, which calculated the results of barrier penetration and diffusion coefficient.

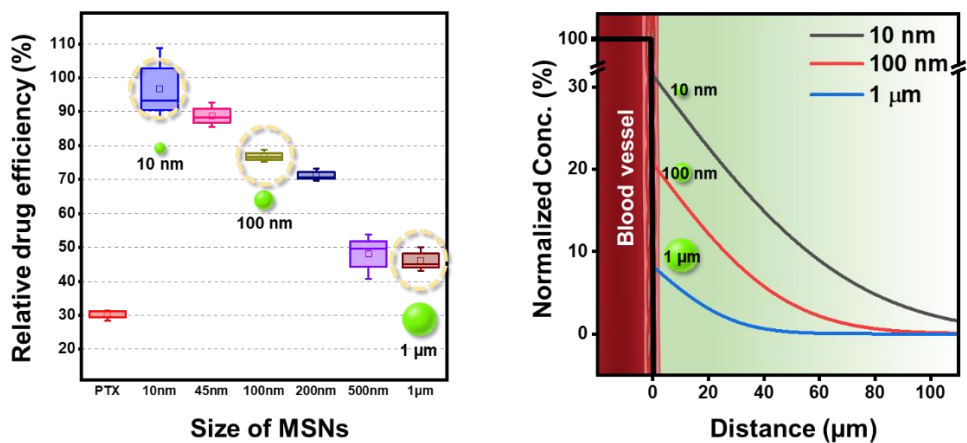


Figure 4.13. Comparing with drug efficiency from animal testing, the modeled system has similar tendency in that the size difference of the particles have different profile as the distance gets farther from the vessel surface.

4.4. Conclusion

I studied barrier penetration and diffusion in both types of chips, and I was able to quantitatively express both of them and even show the combined results. In addition, through comparison with animal experiments, it was confirmed that the actual drug efficiencies and transport tendencies match. Previous chapters did not include blood vessels, but in this study, transport from the inside of blood vessels was studied, and more accurate results were obtained by setting the experiment under conditions that more closely match the Fick's Law boundary conditions. In addition, the reliability of my research was secured through comparison with animal experiments.

Cocultures such as with cancer cells and actual screening tests were not included in this study, but the delivery process was sufficiently simulated through the step-by-step transport research process, and the accuracy was confirmed through comparison with animal experiments. And, by conducting blood vessel research, which plays the most important role in transport research, it is clear that it can be applied to other research, blood brain barrier (BBB) or vascular diseases.

Chapter 5. Conclusion

In each chapter, materials with opposite characteristics, H_2O_2 and MSNs, were used, and diffusion data were fitted to the Pick's law solution based on the characteristics. The diffusion matrix was also used according to each material and situation, and a more complex mixture matrix was used to induce blood vessel formation. In the case of the chip, the study was conducted in a static state at the beginning of the degree course, but later, microfluidics was introduced and the flow rate was set to match the actual blood vessel situation. Blood vessels were formed on the chip and transport from blood vessels was studied.

In conclusion, I researched the transport platform in the form of gradually developing it. The transport process of the biomolecule starting from the surface of the implant and the nanocarrier injected through the circulation system was carried out based on diffusion studies, and quantitative analysis results were also obtained. Basically, to fit the solution of Fick's second law, microfluidics was used, the chip was modified according to the conditions of the equation, and the experimental conditions were set accordingly. It is considered an academically meaningful study because it is a platform that can understand the transport process step by step. It can be used by changing the material and conditions can be changed according to the targeting area, so it is highly utilized and is expected to be used in various research fields.

Through modeling, it is possible to predict the temporal and spatial transmission of materials with opposite characteristics, and it is user-friendly by devising an easy method that anyone can do. Overall, these studies can be used as a screening platform to determine the efficacy of biomolecules (especially drugs), and furthermore, drug-loaded nanoparticles[15, 34, 85, 86]. As new biomaterials are recently developed, it is considered as a platform for testing early material development. In addition, by taking advantage of the fact that materials can be easily changed and used, modeling using co-culture with cancer tissue, spheroids, and organoids can be expected[87]. Through this, when considering animal testing in the future, it is a design that can help animal testing, and can play a complementary role with animal testing[74, 88].

References

1. Arney, D., et al. *Biomedical devices and systems security*. in *2011 Annual International Conference of the IEEE Engineering in Medicine and Biology Society*. 2011.
2. Bhatia, S.N. and D.E. Ingber, *Microfluidic organs-on-chips*. *Nat Biotechnol*, 2014. **32**(8): p. 760-72.
3. Cheng, S.-Y., et al., *A hydrogel-based microfluidic device for the studies of directed cell migration*. *Lab on a Chip*, 2007. **7**(6): p. 763-769.
4. Park, J., et al., *Magnesium Corrosion Triggered Spontaneous Generation of H₂O₂ on Oxidized Titanium for Promoting Angiogenesis*. *Angewandte Chemie International Edition*, 2015. **54**(49): p. 14753-14757.
5. Bharti, C., et al., *Mesoporous silica nanoparticles in target drug delivery system: A review*. *International journal of pharmaceutical investigation*, 2015. **5**(3): p. 124-133.
6. Han, G., A.J. Friedman, and J.M. Friedman, *Nitric Oxide Releasing Nanoparticle Synthesis and Characterization*, in *Nitric Oxide: Methods and Protocols*, H.O. McCarthy and J.A. Coulter, Editors. 2011, Humana Press: Totowa, NJ. p. 187-195.
7. Lee, J.-W., et al., *Long-term clinical study and multiscale analysis of in vivo biodegradation mechanism of Mg alloy*. *Proceedings of the National Academy of Sciences*, 2016. **113**(3): p. 716-721.
8. Fang, J., H. Nakamura, and H. Maeda, *The EPR effect: Unique features of tumor blood vessels for drug delivery, factors involved, and limitations and augmentation of the effect*. *Adv Drug Deliv Rev*, 2011. **63**(3): p. 136-51.
9. LaVan, D.A., T. McGuire, and R. Langer, *Small-scale systems for in vivo drug delivery*. *Nat Biotechnol*, 2003. **21**(10): p. 1184-91.
10. Kim, S., et al., *In-depth study on the gene silencing capability of silica nanoparticles with different pore sizes: degree and duration of RNA interference*. *RSC Advances*, 2016. **6**(32): p. 27143-27150.
11. Hu, T., et al., *Biodegradable stents for coronary artery disease treatment: Recent advances and future perspectives*. *Materials Science and Engineering: C*, 2018. **91**: p. 163-178.
12. Ma, J., N. Zhao, and D. Zhu, *Biphasic responses of human vascular smooth muscle cells to magnesium ion*. *Journal of biomedical materials research. Part A*, 2016. **104**(2): p. 347-356.
13. Park, J., et al., *Tailoring H₂O₂ generation kinetics with magnesium alloys for efficient disinfection on titanium surface*. *Scientific Reports*, 2020. **10**(1): p. 6536.
14. Caballero, D., et al., *Tumour-vessel-on-a-chip models for drug delivery*. *Lab Chip*, 2017. **17**(22): p. 3760-3771.

15. Dittrich, P.S. and A. Manz, *Lab-on-a-chip: microfluidics in drug discovery*. Nature Reviews Drug Discovery, 2006. **5**(3): p. 210-218.
16. Osaki, T., V. Sivathanu, and R.D. Kamm, *Engineered 3D vascular and neuronal networks in a microfluidic platform*. Sci Rep, 2018. **8**(1): p. 5168.
17. Bagulho, A., et al., *The extracellular matrix modulates H₂O₂ degradation and redox signaling in endothelial cells*. Redox Biol, 2015. **6**: p. 454-460.
18. Kilian, K.A., et al., *Geometric cues for directing the differentiation of mesenchymal stem cells*. Proc Natl Acad Sci U S A, 2010. **107**(11): p. 4872-7.
19. Gough, D.R. and T.G. Cotter, *Hydrogen peroxide: a Jekyll and Hyde signalling molecule*. Cell Death Dis, 2011. **2**: p. e213.
20. Katerina Krumova, G.C., *Overview of Reactive Oxygen Species, in Singlet Oxygen: Applications in Biosciences and Nanosciences*. 2016, Royal Society of Chemistry.
21. Winterbourn, C.C., *Reconciling the chemistry and biology of reactive oxygen species*. Nature Chemical Biology, 2008. **4**: p. 278.
22. Kim, J., et al., *Fungal brain infection modelled in a human-neurovascular-unit-on-a-chip with a functional blood–brain barrier*. Nature Biomedical Engineering, 2021.
23. Zhu, M., et al., *In vivo engineered extracellular matrix scaffolds with instructive niches for oriented tissue regeneration*. Nature Communications, 2019. **10**(1): p. 4620.
24. Minchinton, A.I. and I.F. Tannock, *Drug penetration in solid tumours*. Nature Reviews Cancer, 2006. **6**(8): p. 583-592.
25. Raesi, V. and W.C.W. Chan, *Improving nanoparticle diffusion through tumor collagen matrix by photo-thermal gold nanorods*. Nanoscale, 2016. **8**(25): p. 12524-12530.
26. Bini, F., et al., *3D random walk model of diffusion in human Hypo- and Hyper- mineralized collagen fibrils*. Journal of Biomechanics, 2021. **125**: p. 110586.
27. Yang, N., et al., *Manipulate the nano-structure of layered double hydroxides via calcination for enhancing immobilization of anionic dyes on collagen fibers*. Journal of Colloid and Interface Science, 2022. **610**: p. 182-193.
28. Carvalho, T.M.A., et al., *Tumor Microenvironment Features and Chemoresistance in Pancreatic Ductal Adenocarcinoma: Insights into Targeting Physicochemical Barriers and Metabolism as Therapeutic Approaches*. Cancers, 2021. **13**(23): p. 6135.
29. Wong, C.H., K.W. Siah, and A.W. Lo, *Estimation of clinical trial success rates and related parameters*. Biostatistics (Oxford, England), 2019. **20**(2): p. 273-286.
30. Kapalczyńska, M., et al., *2D and 3D cell cultures - a comparison of different types of cancer cell cultures*. Archives of medical science :

- AMS, 2018. **14**(4): p. 910-919.
31. Wang, H.F., et al., *Tumor-Vasculature-on-a-Chip for Investigating Nanoparticle Extravasation and Tumor Accumulation*. ACS Nano, 2018. **12**(11): p. 11600-11609.
32. Jin, Y., et al., *Three-dimensional brain-like microenvironments facilitate the direct reprogramming of fibroblasts into therapeutic neurons*. Nature Biomedical Engineering, 2018. **2**(7): p. 522-539.
33. Lee, S.W.L., et al., *Modeling Nanocarrier Transport across a 3D In Vitro Human Blood-Brain-Barrier Microvasculature*. Adv Healthc Mater, 2020: p. e1901486.
34. Chen, Y.Y., et al., *Clarifying intact 3D tissues on a microfluidic chip for high-throughput structural analysis*. Proc Natl Acad Sci U S A, 2016. **113**(52): p. 14915-14920.
35. Cooksey, G.A., C.G. Sip, and A. Folch, *A multi-purpose microfluidic perfusion system with combinatorial choice of inputs, mixtures, gradient patterns, and flow rates*. Lab on a Chip, 2009. **9**(3): p. 417-426.
36. Baker, B.M., et al., *Microfluidics embedded within extracellular matrix to define vascular architectures and pattern diffusive gradients*. Lab on a chip, 2013. **13**(16): p. 3246-3252.
37. Sapudom, J. and T. Pompe, *Biomimetic tumor microenvironments based on collagen matrices*. Biomater Sci, 2018. **6**(8): p. 2009-2024.
38. Kim, S., et al., *Engineering of functional, perfusable 3D microvascular networks on a chip*. Lab Chip, 2013. **13**(8): p. 1489-500.
39. Hong, X., et al., *The pore size of mesoporous silica nanoparticles regulates their antigen delivery efficiency*. Science Advances, 2020. **6**: p. eaaz4462.
40. Liu, B., et al., *Engineered Interactions with Mesoporous Silica Facilitate Intracellular Delivery of Proteins and Gene Editing*. Nano Letters, 2020. **20**(5): p. 4014-4021.
41. Huang, C., et al., *Robust Nanovaccine Based on Polydopamine-Coated Mesoporous Silica Nanoparticles for Effective Photothermal-Immunotherapy Against Melanoma*. Advanced Functional Materials, 2021. **31**(18): p. 2010637.
42. Manzano, M. and M. Vallet-Regí, *Mesoporous Silica Nanoparticles for Drug Delivery*. Advanced Functional Materials, 2020. **30**(2): p. 1902634.
43. Gisbert-Garzarán, M., et al., *Designing Mesoporous Silica Nanoparticles to Overcome Biological Barriers by Incorporating Targeting and Endosomal Escape*. ACS Applied Materials & Interfaces, 2021. **13**(8): p. 9656-9666.
44. Khan, M.A., et al., *Effect of Confinement in Nanopores on RNA Interactions with Functionalized Mesoporous Silica Nanoparticles*. J Phys Chem B, 2020. **124**(39): p. 8549-8561.

45. Olivieri, F., et al., *Mesoporous silica nanoparticles as carriers of active agents for smart anticorrosive organic coatings: a critical review*. *Nanoscale*, 2021. **13**(20): p. 9091-9111.
46. Halas, N.J., *Nanoscience under Glass: The Versatile Chemistry of Silica Nanostructures*. *ACS Nano*, 2008. **2**(2): p. 179-183.
47. Additives, E. Panel o.F., et al., *Re-evaluation of silicon dioxide (E 551) as a food additive*. *EFSA Journal*, 2018. **16**(1): p. e05088.
48. Janjua, T.I., et al., *Clinical translation of silica nanoparticles*. *Nature Reviews Materials*, 2021. **6**(12): p. 1072-1074.
49. Han, W., et al., *Oriented collagen fibers direct tumor cell intravasation*. *Proceedings of the National Academy of Sciences*, 2016. **113**(40): p. 11208-11213.
50. Yang, Y.L., S. Motte, and L.J. Kaufman, *Pore size variable type I collagen gels and their interaction with glioma cells*. *Biomaterials*, 2010. **31**(21): p. 5678-88.
51. Lieleg, O. and K. Ribbeck, *Biological hydrogels as selective diffusion barriers*. *Trends in Cell Biology*, 2011. **21**(9): p. 543-551.
52. Arends, F., et al., *A microfluidics approach to study the accumulation of molecules at basal lamina interfaces*. *Lab on a Chip*, 2015. **15**(16): p. 3326-3334.
53. Li, L., et al., *A microfluidic in vitro system for the quantitative study of the stomach mucus barrier function*. *Lab on a Chip*, 2012. **12**(20): p. 4071-4079.
54. Lieleg, O., I. Vladescu, and K. Ribbeck, *Characterization of Particle Translocation through Mucin Hydrogels*. *Biophysical Journal*, 2010. **98**(9): p. 1782-1789.
55. Hwang, H.W., et al., *Spatiotemporal Distribution of Mesoporous Silica Nanoparticles in Tissue-Mimicking Collagen Using Lab-on-a-Chip Technology for Drug Carrier Diffusivity Evaluation*. *ACS Applied Nano Materials*, 2022. **5**(9): p. 12435-12443.
56. Kim, S., et al., *Biocompatible N-acetyl-nanoconstruct alleviates lipopolysaccharide-induced acute lung injury in vivo*. *Scientific Reports*, 2021. **11**(1): p. 22662.
57. Bagwe, R.P., L.R. Hilliard, and W. Tan, *Surface modification of silica nanoparticles to reduce aggregation and nonspecific binding*. *Langmuir : the ACS journal of surfaces and colloids*, 2006. **22**(9): p. 4357-4362.
58. Zhu, S., et al., *Fabrication of a novel bio-inspired collagen-polydopamine hydrogel and insights into the formation mechanism for biomedical applications*. *RSC Advances*, 2016. **6**(70): p. 66180-66190.
59. Li, Q., et al., *Polydopamine-collagen complex to enhance the biocompatibility of polydimethylsiloxane substrates for sustaining long-term culture of L929 fibroblasts and tendon stem cells*. *J Biomed Mater Res A*, 2018. **106**(2): p. 408-418.

60. Albanese, A., et al., *Tumour-on-a-chip provides an optical window into nanoparticle tissue transport*. Nature Communications, 2013. **4**(1): p. 2718.
61. Blanco, E., H. Shen, and M. Ferrari, *Principles of nanoparticle design for overcoming biological barriers to drug delivery*. Nature Biotechnology, 2015. **33**(9): p. 941-951.
62. Almeida, J.P., et al., *In vivo biodistribution of nanoparticles*. Nanomedicine (Lond), 2011. **6**(5): p. 815-35.
63. Yang, R., et al., *Getting Drugs Across Biological Barriers*. Advanced Materials, 2017. **29**(37): p. 1606596.
64. Jia, D., et al., *The time, size, viscosity, and temperature dependence of the Brownian motion of polystyrene microspheres*. American Journal of Physics, 2007. **75**(2): p. 111-115.
65. Gensdarmes, F., *Methods of Detection and Characterization*, in *Nanoengineering*. 2015. p. 55-84.
66. Torres-Carbajal, A., S. Herrera-Velarde, and R. Castañeda-Priego, *Brownian motion of a nano-colloidal particle: the role of the solvent*. Physical Chemistry Chemical Physics, 2015. **17**(29): p. 19557-19568.
67. Elacqua, E., et al., *Molecular Recognition in the Colloidal World*. Acc Chem Res, 2017. **50**(11): p. 2756-2766.
68. Wetzel, R.G., *Limnology: Lake and River Ecosystems*. 23 - Detritus: Organic Carbon Cycling and Ecosystem Metabolism. 2001.
69. Slim, A.H., R. Poling-Skutvik, and J.C. Conrad, *Local Confinement Controls Diffusive Nanoparticle Dynamics in Semidilute Polyelectrolyte Solutions*. Langmuir, 2020. **36**(31): p. 9153-9159.
70. Shan, X., S. Wang, and N. Tao, *Study of single particle charge and Brownian motions with surface plasmon resonance*. Appl Phys Lett, 2010. **97**(22): p. 223703.
71. Helminger, G., et al., *Interstitial pH and pO₂ gradients in solid tumors in vivo: High-resolution measurements reveal a lack of correlation*. Nature Medicine, 1997. **3**(2): p. 177-182.
72. Jain, R.K. and L.T. Baxter, *Mechanisms of Heterogeneous Distribution of Monoclonal Antibodies and Other Macromolecules in Tumors: Significance of Elevated Interstitial Pressure*. Cancer Research, 1988. **48**(24 Part 1): p. 7022-7032.
73. Sugihara-Seki, M. and B.M. Fu, *Blood flow and permeability in microvessels*. Fluid Dynamics Research, 2005. **37**(1-2): p. 82-132.
74. Liu, Y., et al., *Narrowing the Gap Between In Vitro and In Vivo Genetic Profiles by Deconvoluting Toxicogenomic Data In Silico*. Frontiers in pharmacology, 2020. **10**: p. 1489-1489.
75. Ehrich, M., *Bridging the Gap between In Vitro and In Vivo Toxicology Testing*. Alternatives to Laboratory Animals, 2003. **31**(3): p. 267-271.
76. Einhorn, T.A. and L.C. Gerstenfeld, *Fracture healing: mechanisms and interventions*. Nat Rev Rheumatol, 2015. **11**(1): p. 45-54.
77. Sackmann, E.K., A.L. Fulton, and D.J. Beebe, *The present and future*

- role of microfluidics in biomedical research*. Nature, 2014. **507**(7491): p. 181-9.
78. Dvorak, H.F., et al., *Fibrin containing gels induce angiogenesis. Implications for tumor stroma generation and wound healing*. Laboratory investigation; a journal of technical methods and pathology, 1987. **57**(6): p. 673-686.
 79. Kattula, S., J.R. Byrnes, and A.S. Wolberg, *Fibrinogen and Fibrin in Hemostasis and Thrombosis*. Arterioscler Thromb Vasc Biol, 2017. **37**(3): p. e13-e21.
 80. Morgan, J.P., et al., *Formation of microvascular networks in vitro*. Nature Protocols, 2013. **8**(9): p. 1820-1836.
 81. Nakatsu, M.N., et al., *Angiogenic sprouting and capillary lumen formation modeled by human umbilical vein endothelial cells (HUVEC) in fibrin gels: the role of fibroblasts and Angiopoietin-1* ☆. Microvascular Research, 2003. **66**(2): p. 102-112.
 82. Saraiva, C., et al., *Nanoparticle-mediated brain drug delivery: Overcoming blood–brain barrier to treat neurodegenerative diseases*. Journal of Controlled Release, 2016. **235**: p. 34-47.
 83. Leung, B.M. and M.V. Sefton, *A modular tissue engineering construct containing smooth muscle cells and endothelial cells*. Ann Biomed Eng, 2007. **35**(12): p. 2039-49.
 84. Dewhirst, M.W. and T.W. Secomb, *Transport of drugs from blood vessels to tumour tissue*. Nature reviews. Cancer, 2017. **17**(12): p. 738-750.
 85. Liu, X., et al., *Tumor-on-a-chip: from bioinspired design to biomedical application*. Microsystems & Nanoengineering, 2021. **7**(1): p. 50.
 86. Zhang, Y., et al., *Utilizing a high-throughput microfluidic platform to study hypoxia-driven mesenchymal-mode cell migration*. Integr Biol (Camb), 2015. **7**(6): p. 672-80.
 87. Ziegler, T., R.W. Alexander, and R.M. Nerem, *An endothelial cell-smooth muscle cell co-culture model for use in the investigation of flow effects on vascular biology*. Annals of Biomedical Engineering, 1995. **23**(3): p. 216-225.
 88. Checkley, S., et al., *Bridging the gap between in vitro and in vivo: Dose and schedule predictions for the ATR inhibitor AZD6738*. Scientific Reports, 2015. **5**(1): p. 13545.

Abstract in Korean

국문 초록

의공학 분야에서 소재의 발달과 활용에 있어 디바이스 기반의 연구, 나노캐리어 활용 등 여러 생체친화소재를 이용한 연구들이 진행되고 있다. 따라서 외부 물질이 체내에 주입되었을 때 그 물질의 거동 이해가 필요하다. 대표적으로 임플란트 재료에서 발생하는 분자단위의 물질들은 매우 국소 부위에서 일어나는 현상으로, 효과를 검증하기 위해서는 발생한 분자들의 시공간적 분포를 이해하여야 하며 혈관으로 주입된 나노캐리어의 경우 일부만이 혈관으로부터 병변까지 도달하므로 병변에 도달하게 되는 양이 실제로 암조직까지 시공간적으로 어떻게 분포하는지 이해하여야 실제로 약물이 전달되는 양을 정확하게 예측할 수 있다. 따라서 이 연구에서는 미세유체칩을 이용하고 재료의 특징을 고려하여 물질의 전달 연구를 할 수 있는 발전된 형태인 *in vitro* 플랫폼을 연구하였다. Solution of Fick's second law에 적용할 수 있는 형태로 칩을 modify 하였으며 microfluidics chip에서 transport 연구를 할 수 있도록 실험을 설계하였다.

첫번째로 특정한 목적을 가지고 체내에 임플란트 된 물질의 표면에서 발생하는 활성산소(ROS)의 거동을 연구하였다. ROS의 화학적 측정 기술을 기반으로 미세유체칩 내부에서 세포외기질 중 하나인 fibrin을 통과하는 과산화수소(H_2O_2)의 농도 측정을 하여 그것의 self-degradation rate을 반영하여 H_2O_2 의 확산 계수를 계산하였다. 또한 단순 fibrin 뿐만 아니라 세포를 포함한 fibrin matrix에서 세포에 의한 consumption 정도를 보여줌으로써 tissue에서 H_2O_2 의 농도 분포를 나타내었고 임플란트 재료 표면에서 발생하는 분자의 시공간적 분포를 예측할 수 있는

플랫폼을 제시하였다.

두번째 연구에서는 또한 미세유체칩을 활용하여 좀 더 활용도가 높은 다공성나노입자(MSN)으로 collagen에서 확산 거동을 연구하였다. 형광물질이 부착된 6개 사이즈의 MSN을 특정 시간에 이미징하는 손쉬운 기법으로 혈류속도를 모사한 flow를 준 칩 내부의 MSN 확산을 포착하였다. 형광 이미지를 토대로 확산계수를 계산하여 수치를 정량적으로 나타내었다. 이를 통해 혈관 바깥으로부터 나노캐리어의 시공간적 분포를 정확한 수치로 예측할 수 있는 플랫폼을 제시하였다.

세번째 연구로는 혈관세포(HUVEC)을 도입하여 주입된 나노캐리어가 실제 혈관에서부터 혈관 벽을 통과하여 확산하는 과정까지 혈관 형성을 위한 5채널 칩과 확산 계산을 위한 3채널 칩을 이용해 모델링을 하였다. 6가지 사이즈 MSN이 혈관 벽을 통과하는지 여부를 확인하고 대표 사이즈 3개의 통과율을 이미지 분석을 통해 계산하였다. 또한 fibrin과 collagen의 혼합 matrix에서 모든 사이즈의 MSN 확산 계수를 앞선 연구와 같은 이미징 분석 방식으로 계산하였다. 여기서 동물실험과의 비교를 통해 이 플랫폼에서 시뮬레이션을 한 결과가 어느정도 경향성이 일치하는 것으로 보아 신뢰성 있는 플랫폼으로 여겨진다.

결론적으로 이 논문은 Fick's second law의 solution에 피팅하여 확산계수를 계산할 수 있도록 미세유체칩을 디자인하고 실험 조건을 세팅함으로써 체외 주입 물질의 transport 연구가 가능하도록 하였다. Transport 과정을 단계적으로 이해할 수 있는 플랫폼이며 다양한 재료를 활용할 수 있다는 점에서 활용도가 높다. Spheroid 또는 organoid 등을 도입하거나 공배양 시스템을 통해 다양한 transport 연구를 진행할 수 있으며, 여러 생체재료가 개발되는 시점에서 개발된 재료의 혈관, 세포외기질 등과의 상호작용 등

초기 스크리닝 테스트를 할 수 있는 플랫폼으로 활용될 수 있을 것으로 기대된다.